Neocortical long-range inhibition promotes cortical synchrony and sleep

Jacob M Ratliff[1§], Geoffrey Terral[1§], Stefano Lutzu[1], Jaime Heiss[2], Julie Mota[1], Bianca Stith[1], Arenski Vazquez Lechuga[1], Charu Ramakrishnan[3], Lief E Fenno[4], Tanya Daigle[5], Karl Deisseroth[3], Hongkui Zeng[5], John Ngai[6], Bosiljka Tasic[5], Lucas Sjulson[1], Stephanie Rudolph[1], Thomas S. Kilduff[2], Renata Batista-Brito[1*]

[1]Albert Einstein College of Medicine, New York City, NY, United States,

[2]Biosciences Division, SRI International, Menlo Park, CA 94025, United States

[3]Stanford University, Stanford, United States,

[4]The University of Texas at Austin, Austin, TX, United States

[5]Allen Institute for Brain Science, Seattle, WA, United States

[6]National Institute of Neurological Disease and Stroke, Bethesda, MD, United States

§These authors are listed as co-first

*Corresponding author

Correspondence should be addressed to: renata.brito@einsteinmed.edu

Abstract:

Behavioral states such as sleep and wake are highly correlated with specific patterns of rhythmic activity in the cortex. During low arousal states such as slow wave sleep, the cortex is synchronized and dominated by low frequency rhythms coordinated across multiple regions. Although recent evidence suggests that GABAergic inhibitory neurons are key players in cortical state modulation, the *in vivo* circuit mechanisms coordinating synchronized activity among local and distant neocortical networks are not well understood. Here, we show that somatostatin and chondrolectin co-expressing cells (Sst-Chodl cells), a sparse and unique class of neocortical inhibitory neurons, are selectively active during low arousal states and are largely silent during periods of high arousal. In contrast to other neocortical inhibitory neurons, we show these neurons have long-range axons that project across neocortical areas. Activation of Sst-Chodl cells is sufficient to promote synchronized cortical states characteristic of low arousal, with increased spike co-firing and low frequency brain rhythms, and to alter behavioral states by promoting sleep. Contrary to the prevailing belief that sleep is exclusively driven by subcortical mechanisms, our findings reveal that these long-range inhibitory neurons not only track changes in behavioral state but are sufficient to induce both sleep-like cortical states and sleep behavior, establishing a crucial circuit component in regulating behavioral states.

Introduction

Mammals spend much of their day in sleep and other states of rest. Regular rest activity is instrumental for metabolism, hormone regulation, learning, positive emotion, attention, immune health, and other essential functions [1–6]. The inability to regulate states of restfulness disrupts an animal's ability to function and is associated with a variety of pathologies such as insomnia, sleep apnea, narcolepsy, depression, ADHD, schizophrenia, and even death [6–15]. Transitions between alertness and low arousal states, such as quiet wakefulness and sleep occur over a period of seconds and the resulting states are highly correlated with specific rhythmic activity patterns in the neocortex (i.e., oscillatory activity or cortical states) [16–19]. Periods of low arousal, such as slow wave sleep (SWS) or quiet immobility, are dominated by low frequency fluctuations and spiking co-activation patterns in the cortex termed *synchronized states.* Synchronized, low arousal states alternate with periods of high arousal and active behaviors during which low frequency cortical fluctuations are suppressed and are termed *desynchronized states* [16,17]. GABAergic inhibitory neurons (INs) have been repeatedly suggested as regulators of arousal state-dependent neocortical activity [20–25] with fast-spiking parvalbumin-expressing IN cells demonstrated to promote desynchronized states [26,27]. In contrast, little is known about the function of other INs in the control of synchronized states [25]. Here, we show that a small, distinct class of neocortical INs are selectively active during periods of low arousal, when cortical networks are synchronized, and that activation of these neurons is sufficient to promote synchronous neocortical activity and sleep.

Although it has been known for nearly a century that cortical INs are highly diverse [28], assigning a function to individual neuronal classes has proven difficult, in part because currently established neuronal classes are highly heterogeneous [29–31]. For example, somatostatin (Sst) expressing cells, which are often treated as a monolithic group, can be subdivided into >10 subclasses with distinct morpho-electric and transcriptomic properties [24,29,30,32–34]. Here, we investigate the functional role of a homogenous and unique transcriptomic subtype of Sst INs characterized by the co-expression of Sst, chondrolectin (Chodl), neuronal nitric oxide synthase (Nos1), and the Neurokinin-1 receptor (Tacr1); hereinafter called Sst-Chodl cells as previously described [30,32,33]. These Sst-Chodl cells are GABAergic, but, unlike the canonical locally-projecting neocortical INs, they are long-range projecting cells with axons that in mice can spread over millimeters and across centimeters in larger brains [35–39]. Sst-Chodl cells likely play an essential role in brain function and behavior, because, despite their sparsity (<1% of GABAergic cortical neurons) [33,40] and the high energetic cost to maintain their projections, they are evolutionarily conserved across species from salamanders to humans [41,42]. Previous *ex vivo* work has indicated that Sst-Chodl cells are likely active during SWS [43–46], raising a potential relationship between the activity of these cells and synchronized states. However, the activity and function of Sst-Chodl cells *in vivo* has remained difficult to investigate due to the lack of tools to target, manipulate, and monitor them specifically.

Here, we utilize an intersectional genetic strategy [47–49] to selectively target Sst-Chodl cells and test their functional role. We find that these neurons make dense regional and inter-areal neocortical connections and are active during periods of high cortical synchrony, specifically during quiet wakefulness and SWS. Activation of Sst-Chodl cells drives neocortical activity towards a sleep-like cortical state defined by prominent neocortical synchrony, and activation of these cells across the entire neocortex promotes sleep. Therefore, by tracking and causing changes in neocortical synchronization states, Sst-Chodl cells are ideally positioned to coordinate

state-dependent network activity and subsequent associated behaviors. In contrast to dominant theories suggesting that sleep is generated subcortically, involving the cortex only as a passive follower [50], this work demonstrates that the activity of a specific subclass of neocortical INs, the Sst-ChodI cells, is sufficient to generate low-arousal cortical states and sleep.

Results

Sst-ChodI cells are long-range inhibitory neurons with dense projections

We used intersectional genetics to selectively target Sst-ChodI cells (Fig 1a, Supp Fig 1). Single cell sequencing showed that while only about 24% of cells labelled with $Nos1^{creER}$ mouse line were Sst-ChodI cells, the double transgenic mouse lines which combined Sst^{flp} and $Chodl^{cre}$ or Sst^{flp} and $Nos1^{creER}$ showed similar high specificity in Sst-ChodI targeting (Fig 1a) [49]. We confirmed with immunohistochemistry that this strategy yielded specific and high expression in Sst-ChodI cells (Supp Fig 1d-e).

Next, to evaluate the extent of Sst-ChodI cell projections, we injected the intersectional AAV8-Ef1a-CreOn/FlpOn-oScarlet vector into the primary visual cortex (V1) of Sst^{flp} and $Nos1^{creER}$ double transgenic intersectional mice ("Sst^{flp} ; $Nos1^{creER}$ mice"; Supp Fig 1c-d) to express a bright, cell filling fluorophore. We then took sagittal sections of the full brain, sampling uniformly, and aligned sections to the Allen Institute Common Coordinate Framework (see Methods, Fig 1b). This procedure allowed us to annotate the oScarlet-labelled arbor of Sst-ChodI cells across the brain (Fig 1b-d). We found that Sst-ChodI cells were present in all layers and had dense regional (within visual areas) arborizations (200-600 mm of arbor per mm^3 of tissue), likely comprised of axons and dendrites, in addition to long-range projections (10-50 mm of arbor per mm^3 of tissue), which likely consisted of axons (Fig 1d-e, Supp Fig 2a-b). While the regional projections span across layers, the long-range, inter-areal projections preferentially travelled through upper layers (Fig 1e). These inter-areal projections travelled broadly across ipsilateral neocortex (with a small projection to contralateral cortex) and densely innervated visual areas (Fig 1f), with the most dense innervations targeting V1 and the rostrolateral visual area (Area RL) (Fig 1g). However, these cells had a non-uniform spread of arbor as the anterior visual area (Area A) adjacent to densely innervated areas had some of the least dense arborization among visual areas (Fig 1g). Sst-ChodI cells also had inter-areal projections (Supp Fig 2c-e) targeting most of the neocortex, including retrosplenial, auditory, somatosensory, and frontal motor areas (Fig 1h) with only far anterior and dorsal neocortical regions lacking any projections (agranular insular area, frontal pole, gustatory areas, infralimbic area, orbital area). Outside of the neocortex, we found a small but consistent projection from V1 Sst-ChodI cells to the ipsilateral subiculum but no projections to other non-neocortical areas (Fig 1h, Supp Table 1).

Using whole brain tissue clearing and light sheet imaging, we compared the arborization patterns from animals with cells labelled in V1 and cells labelled in primary somatosensory cortex (S1) (Supp Fig 3, Supp Movie 1). Similarly to cells in V1, we found that cells in S1 had dense arbors spanning all layers within the injected regions and long-range interareal projections travelling preferentially through superficial layers (Supp Fig 3b-f). Those projections were ipsilateral, staying within the neocortex (Supp Fig 3b-g). While inter-areal projections from V1 Sst-ChodI cells extensively targeted retrosplenial areas, the long-range projections of S1 Sst-ChodI cells more densely innervated areas surrounding the injection site such as frontal, motor and visual areas (Supp Fig 3b-g).

These data demonstrate that Sst-ChodI cells from distinct neocortical areas have the common feature of being long-range projecting cells that widely target the ipsilateral neocortex.

Sst-ChodI cells target most neurons across all neocortical layers

To further investigate the neocortical synaptic targets of Sst-ChodI cells, we expressed channelrhodopsin-2 in Sst-ChodI cells by injecting AAVdj CreOn/FlpOn ChR2-EYFP into V1 of Sst^{flp} ; $Nos1^{creER}$ mice, and performed whole-cell patch-clamp recordings in putative post-synaptic cells across all layers of V1 (Supp Fig 4a). Using brief pulses of whole-field blue light stimulation (0.5 ms/ 473 nm), we found that optogenetically-evoked inhibitory postsynaptic currents (oIPSCs) were obtained in nearly all cells from all layers except for layer II/III where 8 of 14 cells (57%) responded to Sst-ChodI cell stimulation (Supp. Fig. 4b). The post-synaptic targets of Sst-ChodI cells included both pyramidal neurons and interneurons (Supp Fig 4a, c). We confirmed that these currents were monosynaptic and mediated by the $GABA_A$ receptor as they persisted in presence of a cocktail of tetrodotoxin and 4-aminopyridine and were blocked by $GABA_A$ receptor antagonist gabazine (50 µM) (Supp Fig 4d-e). Finally, the response amplitude differed between layers with significantly larger oIPSCs in layer VI as compared to other layers (Supp. Fig 4b-c).

These data align with our anatomical findings and indicate that Sst-ChodI cells exert broad inhibition across all layers of V1.

Sst-ChodI cells are active during periods of low-arousal and high neocortical synchrony

To test whether Sst-ChodI cell activity changes across sleep and wake states as suggested by previous c-Fos studies [45,46], we expressed a GCaMP calcium indicator (either via viral vector or transgenic line, see Methods) using Sst^{flp} ; $Nos1^{creER}$ or Sst^{flp} ; $ChodI^{cre}$ mice. We then used 2-photon calcium imaging to observe the patterns of activation of labelled cells during different arousal and synchronization states measured by pupillometry, locomotion, contralateral cortical local field potentials (LFPs) – specifically the delta (1-4Hz) band – electromyography (EMG), and facial movements (Fig 2a-b, Supp Movie 2). Since these state measurements had consistent relationships (Supp Fig 5a), we combined them into a 1-dimensional “Arousal Score”, which corresponds to the first principal component of these state measurements (Fig 2b, Supp Fig 5b).

To facilitate the occurrence of sleep, we extensively habituated mice to head fixation and the imaging setup (see Methods). We scored sleep states automatically [51,52] with subsequent manual curation. Using our state measurements, we were able to classify the animals’ state into four categories: awake states that we further divided into periods of Movement and Quiet Wakefulness (Quiet Wake or QW), SWS, and Rapid Eye Movement (REM) sleep (Fig 2b). Wakefulness was characterized by high EMG and low delta power/power spectral slope with Movement discriminated by periods of high locomotion and facial movements whereas Quiet Wake by periods of virtually absent motion; SWS was characterized by low EMG and high delta power/power spectral slope; and REM sleep was characterized by low EMG and high theta power [51,52].

We found that a large proportion of labelled Sst-ChodI cells from both intersectional mouse lines had intense activity during periods of low arousal and high synchrony such as SWS and Quiet Wake, and their activity was highly suppressed during REM sleep and Movement (95 out of 111

cells; Fig 2c), when the neocortex is desynchronized. This cell population also changed its activity in conjunction with the transitions between states (Fig 2d). When mice ceased locomotion, these cells gradually increased their activity alongside a decrease in arousal levels. As mice entered SWS, the activity of these cells rapidly increased and remained high during the sleep bout. Finally, as mice transitioned from SWS to REM sleep, their activity was sharply suppressed (Fig 2d). We also found a small proportion of labeled cells with opposite pattern of activation largely from the Sst^{flp} ; $Nos1^{creER}$ cross (active during high movement; 16 out of 111 cells) (Supp Fig 5c-e). This population is consistent with our sequencing and immunohistochemistry results showing a small proportion of non-Sst-ChodI cells within both intersectional crosses and with a previously described small heterogenous population of non-Sst-ChodI cells that express Sst and Nos1 [32,53] (Supp Fig 5e).

We examined the consistency of the activity patterns of Sst-ChodI cells whose activity was correlated with low arousal. We found that this population was remarkably homogenous with cells showing strong positive correlations with low arousal metrics including spectral power in the delta band and time elapsed since last locomotion (i.e., stillness duration) and, conversely, negative correlations with measures of high arousal such as EMG, facial motion, locomotion and pupil diameter. The activity among these cells was also highly correlated and dependent upon the arousal level of the animal with cells more correlated in low arousal states (Fig 2b, d-f). Finally, we divided LFP signatures between periods of high and low activity of recorded cells and found that these neurons were most active when cortical networks were highly synchronized (i.e., high delta power; Fig 2g-h).

To evaluate the specificity of Sst-ChodI cell activity patterns, we compared their activity to that of the larger Sst population using publicly available data from the Allen Brain Observatory (Supp Fig 6a). We examined the correlation of Sst cells with arousal states using the locomotion and pupil area state metrics available in the dataset. We found that the Sst population was largely correlated with increased arousal (Supp Fig 6b-d) but with a small population of arousal anti-correlated cells (Supp Fig 6d-e). Interestingly, the proportion of arousal anti-correlated cells in the Sst population was roughly similar to the proportion of Sst-ChodI cells within the Sst population, suggesting that the anti-correlated cells consist of Sst-ChodI cells: 6 out of 147 cells (4%) from the Allen Brain Observatory imaging dataset and 25 out of 900 cells (3%) from the Allen Brain Science patch-seq data set (Supp Fig 6e – see Methods).

Together, our results suggest that, unlike other Sst cells, Sst-ChodI cell activity tracks changes in behavioral/arousal states with increased activity during the state characterized by high cortical synchrony.

Activation of Sst-ChodI cells induces neocortical synchrony

To test for a causal relationship between Sst-ChodI cell activity and neocortical synchrony, we optogenetically activated these cells while performing high density electrophysiological recordings in head-fixed animals (Fig 3a). We acutely inserted 64-channel linear silicon probes with attached tapered optical fibers into the V1 of mice which virally expressed ChR2 in Sst-ChodI cells (Fig 3a). This approach allowed us to simultaneously stimulate neocortical Sst-ChodI cells with light while recording neocortical LFP and single units across layers (Fig 3b). Stimulation occurred in blocks lasting approximately 30 min interspersed with blocks without stimulation (spontaneous blocks, see Methods). Stimulation blocks were further divided between periods of stimulation and inter-

trial intervals (ITI) each lasting 30 sec (Fig 3c). We examined multiple metrics of the synchronized state combining data from LFP and spiking activity to determine the level of cortical synchrony with and without Sst-ChodI cell stimulation (Fig 3d-k).

First, we compared power spectra across depths in V1 between optogenetic stimulation and spontaneous periods. We found increased delta band power, which is characteristic of a synchronized cortical state, across all layers with the most prominent increase found in deeper layers (Fig 3d). Dividing the data according to state, stimulation of Sst-ChodI cells significantly increased delta-band LFP power during both SWS and QW (states when Sst-ChodI cells are typically active; REM sleep bouts were omitted due to insufficient duration). There was also a trend toward increased delta power during Movement (Fig 3d, Supp Fig 7a-b).

Then, we examined spiking synchrony of well-isolated single units (putative single neurons) in response to activation of Sst-ChodI cells. We calculated the spike train cross correlation of single unit pairs and found that stimulation increased the magnitude of spiking synchrony when comparing ITI to stimulation periods (Fig 3e), independent of the stimulation frequencies (Supp Fig 7c-e) or regular spiking *vs* fast spiking cell type (Fig 3e, Supp Fig 7f). When assessed across behavioral states, consistent increases in spiking synchrony occurred with Sst-ChodI cell stimulation during SWS, QW, and even Movement periods when Sst-ChodI cells were not spontaneously active (Fig 3f, Supp Fig 7g-h). We analyzed the impact of Sst-ChodI cell stimulation on the population firing rate and found a small decrease in the population firing rate (Supp Fig 7i-k), indicating that the increase of spiking synchrony cannot be explained by a rise in spiking activity but instead results from a change in temporal spiking patterns.

As LFP patterns and spiking activity are intimately related, we assessed the relationship between the ongoing LFP fluctuations and the timing of spiking activity during stimulation, specifically determining the phase locking value to quantify spike-field coherence. Spikes typically showed a strong locking to the delta band of the LFP (Fig 3g). Stimulation of Sst-ChodI cells strongly accentuated this effect, with increased spiking coherence with delta band LFP fluctuations (Fig 3g, h) as can be observed with increased levels of endogenous cortical synchrony. Another extreme example of phase locking is the DOWN states which consist of brief periods of near-total absence of spiking during an upward deflection of the cortical LFP with enhanced spiking and are a feature of low-arousal cortical states, particularly SWS [54]. We found that DOWN states were more pronounced during optogenetic stimulation of Sst-ChodI cells as both the amplitude and duration of these DOWN states increased (Fig 3i-k, Supp. Fig 7l, m).

Lastly, we investigated whether the activation of Sst-ChodI cells could facilitate widespread intracortical synchronization in freely-moving animals. We generated transgenic mice that expressed the excitatory opsin, CatCh [55], in Sst-ChodI cells and implanted EEG and EMG leads alongside 5 blue LEDs onto the skull of each mouse above thinned bone. We found that stimulation with repeated 1 second rectangular light pulses for periods of 1h specifically increased delta power during SWS (Supp. Fig. 8), indicating that global activation of neocortical Sst-ChodI cells promotes global cortical synchronization.

Taken together, these data suggest that stimulation of Sst-ChodI cells increased synchronization within cortical networks, thereby mimicking features of endogenous cortical synchrony observed during SWS.

Neocortical activation of Sst-ChodI cells promotes sleep

Previous work has suggested that during intense SWS periods (characterized by intense cortical synchrony), putative Sst-ChodI cells are active throughout the neocortex (Gerashchenko et al. 2008). Since stimulation of Sst-ChodI cells generated a synchronized neocortical state reminiscent of SWS (Fig. 3 and Supp. Fig 7-8), we hypothesized that activation of Sst-ChodI cells throughout the whole neocortex would induce not only cortical synchrony but also behavioral features of sleep. To test this hypothesis, we utilized a chemogenetic approach in Sst^{flp} ; $Nos1^{creER}$ mice that were bilaterally injected with AAV8-CreOn/FlpOn-hM3Dq-mCherry vector in 22 neocortical location (11 injections/hemisphere) to express an excitatory DREADD in Sst-ChodI cells (Fig. 4a, Supp. Fig. 9a,b). A systemic injection of a low concentration of the DREADD receptor agonist, clozapine-N-oxide (CNO, 0.5 mg/kg) increased the activity of Sst-ChodI cells, whereas vehicle injection had no effect (Supp. Fig. 9c, Supp Movie 2, 3). To test the impact of pan-neocortical activation of Sst-ChodI cells on sleep behavior, we performed counterbalanced systemic injections of either vehicle or CNO and recorded the LFP and movement of mice in their home cage (Fig. 4b, Supp. Fig. 9a). Activation of Sst-ChodI cells with systemic injection of CNO promoted both SWS and REM sleep relative to vehicle (Fig. 4b-d, Supp. Fig. 9d). Although the number of SWS bouts did not change significantly, DREADD-mediated Sst-ChodI cell activation reduced the latency to sleep and increased the duration of SWS bouts (Fig. 4e,f, Supp. Fig. 9e).

We used DeepLabCut [56] to determine the distance the mice travelled and duration in the nest following global activation of neocortical Sst-ChodI cells. We found that CNO-injected mice moved less and spent more time in the nest, consistent with the increase in sleep induced by activation of Sst-ChodI cells (Fig. 4g,h, Supp. Fig. 9f).

Finally, we examined the impact of pan-neocortical activation of Sst-ChodI cells on LFP signals recorded in the neocortex and the hippocampus. Similarly to optogenetic manipulation (Fig. 3d, Supp. Fig 7-8), chemogenetic activation of the neocortical Sst-ChodI cells induced an increase in neocortical LFP power mainly for low frequency bands during both SWS and WAKE states. This effect was specific to the neocortex as it was not observed in the hippocampus (Fig. 4i,j, Supp. Fig. 10a), suggesting that Sst-ChodI cell activation preferentially impacted neocortical circuits. Importantly, CNO treatment in control mice that did not express DREADD receptors neither altered sleep/wake states (Supp. Fig. 9g) nor LFP signals (Supp. Fig. 10b).

Altogether, our results indicate that global activation of neocortical Sst-ChodI cells is sufficient to promote cortical synchrony and sleep.

Discussion

We have shown that long-range, neocortical Sst-ChodI cells – a unique neuronal subtype [30,36] that is highly conserved across evolution [33,41,42] – are selectively active during low arousal synchronized states and are a key player in promoting patterns of synchronous neocortical activity. We propose that activation of their dense local and long-range projections synchronize neocortical networks, thereby driving the animal's state towards SWS.

Cortical synchronization states are generated by the interactions of a variety of cell types and circuit components within and outside of the cortex. In particular, previous work has shown that cortical fast-spiking parvalbumin-expressing cells are critical for the generation of desynchronized states by enhancing gamma oscillations [26,27]. In contrast, we have shown here that the activity of Sst-ChodI cells not only track the synchronization states but also dynamically promote these

states, enhancing delta frequency LFP fluctuations and spiking co-activation. We have also demonstrated that Sst-ChodI cells have extremely dense projections and high synaptic connectivity across all layers within the cortical region where their cell bodies are located, making them excellent candidates to promote local cortical synchrony. This feature could be important for local sleep, where local regions exhibit sleep-like patterns in absence of behavioral sleep [57]. We also have shown that Sst-ChodI cells have long-range projections, making them ideal candidates for regulating the precise synchrony observed across long distances in the neocortex [58].

The dominant hypothesis for the neural regulation of sleep proposes that subcortical structures control the initiation, generation, and maintenance of sleep, with the cortex merely as a passive follower [50]. More recent work has begun to explore the active role of the neocortex in regulating sleep/wake states in a top-down manner. In particular, a subset of cortical Sst-expressing cells have been proposed to promote sleep and control sleep preparatory behavior [59,60]. However, it remains to be determined whether those Sst cells correspond to the Sst-ChodI neurons. Future studies will be required to analyze the projection pattern of Sst-ChodI cells in detail outside sensory areas to determine whether these neurons project to canonical sleep-promoting regions in the hypothalamus. It is also possible that Sst-ChodI neurons control general cortical synchronization and arousal state by regulating the activity of cortical pyramidal neurons. Indeed, a cortex-wide reduction of the synaptic outputs from pyramidal cells in deep layers has been shown to reduce homeostatic sleep rebound [61]. We have demonstrated that Sst-ChodI neurons provide particularly strong synaptic inhibition to - and LFP modulation onto - deep cortical layers where pyramidal cells relevant for synchronized states are located [62–64]. These observations suggest that activation of Sst-ChodI cells could regulate sleep homeostasis primarily by modulating deep layer pyramidal cells. In fact, previous *ex vivo* work suggests that putative Sst-ChodI cells are likely relevant for homeostatic recovery from sleep deprivation [45,46], an interaction that is still not well understood and would be interesting to investigate in subsequent studies.

While cortical Sst-expressing cells as a whole have been proposed to regulate sleep features [59,60], their functional role has been hard to assess, with different studies coming to different conclusions. This discrepancy is reflected in the brain rhythms regulated and/or generated by Sst cells including gamma rhythms [65,66], beta rhythms [67], theta rhythms [68], and delta rhythms [59]. Single-cell transcriptomic profiling has revealed that the Sst neurons can be divided into multiple subclasses with different functions [24,32]. Therefore, different subclasses of Sst cells may regulate opposing functions and brain rhythms; consequently, the functional outcomes from previous studies may depend on the different experimental methods that differentially engage these neuronal subtypes. In agreement with this idea, we also identified a small proportion of cells within the Sst and Nos1 intersection that are anti-corelated with arousal states and likely represent non-Sst-ChodI, Type II Nos1 cells that express low levels of Sst and Nos1 [32,53] and may be involved in neurovascular control during movement [37,43,69]. Our study demonstrates the utility of leveraging transcriptomic profiling in targeting IN subclasses and understanding brain function, an approach that can be used to further investigate the function of other Sst neuronal IN subclasses.

In addition to the inhibitory function of Sst-ChodI cells on downstream neuronal targets, other neurotransmitters expressed by these neurons could be relevant for their function. Of note, Sst-ChodI neurons likely serve as the largest source of NO signaling in the neocortex [48]. Mice deficient in Nos1 have reduced sleep due to the inability to sustain long SWS bouts and exhibit excessive sleepiness, yet, in the absence of NO, these mice are unable to mount a homeostatic response

to sleep deprivation [45]. Mice lacking Nos1 specifically in Sst cells also have a deficit in delta rhythms [70]. Putative targets of NO signaling from Sst-ChodI cells include parvalbumin-expressing cells [48,71] and the neurovascular system [37,69]. The slow synchronized electrical rhythm generated by Sst-ChodI neuronal activation may be mirrored in the cells of the neurovascular system to support the rhythmic fluid movement during glymphatic clearance from the brain during sleep [72,73].

The mechanisms underlying the suppression of Sst-ChodI cells during desynchronized cortical activity and the activation of these cells during synchronized states, such as SWS, remain to be determined. It is possible that the activation of Sst-ChodI cells during synchronized states is caused by release of inhibition from arousal-related neuromodulators, such as acetylcholine [74], similar to arousal anti-correlated cells in the hippocampus [75]. This is consistent with previous studies showing that Sst-ChodI cells strongly express inhibitory muscarinic M2 and M4 receptors as well as inhibitory 5HT1a receptors [30,48,74,76]. Another possibility is that sleep-promoting substances (somnogens), such as adenosine, could stimulate these cells during synchronized states [43]. Substance P activates Sst-ChodI cells and local injections of Substance P have been shown to promote cortical slow-wave activity and cortical signatures of SWS [44,70,74], though its link to sleep is not fully understood [77]. Identifying additional G-protein coupled receptors expressed by Sst-ChodI neurons will help understand sleep and wake related signaling pathways.

Overall, this work highlights a crucial circuit element in the regulation of low arousal neocortical states and sleep. The function of this cortical cell type, the Sst-ChodI cells, challenges the notion of subcortical hegemony in sleep generation and, along with other studies, highlights an underappreciated role played by the cortex in sleep control. Since sleep is disrupted in a variety of neuropsychiatric, neurodevelopmental and neurological disorders, this highly conserved, genetically distinct cell class may serve as a potential therapeutic target in future studies.

References

1. Anafi, R. C., Kayser, M. S. & Raizen, D. M. Exploring phylogeny to find the function of sleep. *Nat Rev Neurosci* **20**, 109–116 (2019).

2. Bryant, P. A., Trinder, J. & Curtis, N. Sick and tired: Does sleep have a vital role in the immune system? *Nat Rev Immunol* **4**, 457–67 (2004).

3. Rasch, B. & Born, J. About sleep's role in memory. *Physiol Rev* **93**, 681–766 (2013).

4. Rechtschaffen, A., Gilliland, M. A., Bergmann, B. M. & Winter, J. B. Physiological correlates of prolonged sleep deprivation in rats. *Science* **221**, 182–4 (1983).

5. Iwanczuk, W. & Guzniczak, P. Neurophysiological foundations of sleep, arousal, awareness and consciousness phenomena. Part 2. *Anaesthesiol Intensive Ther* **47**, 168–74 (2015).

6. Vaccaro, A. *et al.* Sleep Loss Can Cause Death through Accumulation of Reactive Oxygen Species in the Gut. *Cell* **181**, 1307-1328.e15 (2020).
7. Gisabella, B., Babu, J., Valeri, J., Rexrode, L. & Pantazopoulos, H. Sleep and Memory Consolidation Dysfunction in Psychiatric Disorders: Evidence for the Involvement of Extracellular Matrix Molecules. *Front Neurosci* **15**, 646678 (2021).
8. Geoffroy, P. A. *et al.* Sleep complaints are associated with increased suicide risk independently of psychiatric disorders: results from a national 3-year prospective study. *Mol Psychiatry* **26**, 2126–2136 (2021).
9. Neisewander, J. L. Sleep Deprivation Dysregulates Brain Reward Circuitry: Implications for Psychiatric Disorders. *Biol Psychiatry* **87**, 938–939 (2020).
10. Geoffroy, P. A., Tebeka, S., Blanco, C., Dubertret, C. & Le Strat, Y. Shorter and longer durations of sleep are associated with an increased twelve-month prevalence of psychiatric and substance use disorders: Findings from a nationally representative survey of US adults (NESARC-III). *J Psychiatr Res* **124**, 34–41 (2020).
11. Freeman, D., Sheaves, B., Waite, F., Harvey, A. G. & Harrison, P. J. Sleep disturbance and psychiatric disorders. *Lancet Psychiatry* **7**, 628–637 (2020).
12. Kaskie, R. E. & Ferrarelli, F. Sleep disturbances in schizophrenia: what we know, what still needs to be done. *Curr Opin Psychol* **34**, 68–71 (2019).
13. Hombali, A. *et al.* Prevalence and correlates of sleep disorder symptoms in psychiatric disorders. *Psychiatry Res* **279**, 116–122 (2019).
14. Cox, R. C. & Olatunji, B. O. A systematic review of sleep disturbance in anxiety and related disorders. *J Anxiety Disord* **37**, 104–29 (2016).
15. Rumble, M. E., White, K. H. & Benca, R. M. Sleep Disturbances in Mood Disorders. *Psychiatr Clin North Am* **38**, 743–59 (2015).

16. Poulet, J. F. A. & Crochet, S. The Cortical States of Wakefulness. *Front. Syst. Neurosci.* **12**, (2019).
17. Harris, K. D. & Thiele, A. Cortical state and attention. *Nat. Rev. Neurosci.* **12**, 509–523 (2011).
18. McGinley, M. J. *et al.* Waking State: Rapid Variations Modulate Neural and Behavioral Responses. *Neuron* vol. 87 1143–1161 (2015).
19. Vinck, M., Batista-Brito, R., Knoblich, U. & Cardin, J. A. Arousal and Locomotion Make Distinct Contributions to Cortical Activity Patterns and Visual Encoding. *Neuron* **86**, 740–754 (2015).
20. Batista-Brito, R., Zagha, E., Ratliff, J. M. & Vinck, M. Modulation of cortical circuits by top-down processing and arousal state in health and disease. *Current Opinion in Neurobiology* vol. 52 172–181 (2018).
21. Cardin, J. A. Inhibitory Interneurons Regulate Temporal Precision and Correlations in Cortical Circuits. *Trends in Neurosciences* vol. 41 689–700 (2018).
22. Batista-Brito, R. *et al.* Developmental Dysfunction of VIP Interneurons Impairs Cortical Circuits. *Neuron* **95**, 884-895.e9 (2017).
23. Fishell, G. & Rudy, B. Mechanisms of Inhibition within the Telencephalon: "Where the Wild Things Are". *Annu. Rev. Neurosci.* **34**, 535–567 (2011).
24. Bugeon, S. *et al.* A transcriptomic axis predicts state modulation of cortical interneurons. *Nature* **607**, 330–338 (2022).
25. Roux, L. & Buzsáki, G. Tasks for inhibitory interneurons in intact brain circuits. *Neuropharmacology* **88**, 10–23 (2015).
26. Cardin, J. A. *et al.* Driving fast-spiking cells induces gamma rhythm and controls sensory responses. *Nature* **459**, 663–667 (2009).
27. Sohal, V. S., Zhang, F., Yizhar, O. & Deisseroth, K. Parvalbumin neurons and gamma rhythms enhance cortical circuit performance. *Nature* **459**, 698–702 (2009).
28. Ramon y Cajal, S. *Recollections of My Life*. (The MIT Press, Cambridge, MA, 1937).

29. Zeisel, A. *et al.* Cell types in the mouse cortex and hippocampus revealed by single-cell RNA-seq. *Science* **347**, 1138–1142 (2015).
30. Tasic, B. *et al.* Adult mouse cortical cell taxonomy revealed by single cell transcriptomics. *Nat. Neurosci.* **19**, 335–346 (2016).
31. Rudy, B., Fishell, G., Lee, S. H. & Hjerling-Leffler, J. Three groups of interneurons account for nearly 100% of neocortical GABAergic neurons. *Dev. Neurobiol.* **71**, 45–61 (2011).
32. Gouwens, N. W. *et al.* Integrated Morphoelectric and Transcriptomic Classification of Cortical GABAergic Cells. *Cell* **183**, 935-953.e19 (2020).
33. Yao, Z. *et al.* A taxonomy of transcriptomic cell types across the isocortex and hippocampal formation. *Cell* **184**, 3222-3241.e26 (2021).
34. Wu, S. J. *et al.* Cortical somatostatin interneuron subtypes form cell-type-specific circuits. *Neuron* **111**, 2675-2692.e9 (2023).
35. Tomioka, R. *et al.* Demonstration of long-range GABAergic connections distributed throughout the mouse neocortex. *Eur. J. Neurosci.* **21**, 1587–1600 (2005).
36. Fisher, J. *et al.* Cortical somatostatin long-range projection neurons and interneurons exhibit divergent developmental trajectories. *Neuron* (2023) doi:10.1016/j.neuron.2023.11.013.
37. Ruff, C. F. *et al.* Long-range inhibitory neurons mediate cortical neurovascular coupling. *Cell Rep.* **43**, 113970 (2024).
38. Tomioka, R. & Rockland, K. S. Long-distance corticocortical GABAergic neurons in the adult monkey white and gray matter. *J. Comp. Neurol.* **505**, 526–538 (2007).
39. He, M. *et al.* Strategies and Tools for Combinatorial Targeting of GABAergic Neurons in Mouse Cerebral Cortex. *Neuron* **91**, 1228–1243 (2016).
40. Krienen, F. M. *et al.* Innovations present in the primate interneuron repertoire. *Nature* **586**, 262–269 (2020).

41. Woych, J. *et al.* Cell-type profiling in salamanders identifies innovations in vertebrate forebrain evolution. *Science* **377**, eabp9186 (2022).
42. Hodge, R. D. *et al.* Conserved cell types with divergent features in human versus mouse cortex. *Nature* **573**, 61–68 (2019).
43. Kilduff, T. S., Cauli, B. & Gerashchenko, D. Activation of cortical interneurons during sleep: An anatomical link to homeostatic sleep regulation? *Trends in Neurosciences* vol. 34 10–19 (2011).
44. Dittrich, L., Morairty, S. R., Warrier, D. R. & Kilduff, T. S. Homeostatic sleep pressure is the primary factor for activation of cortical nNOS/NK1 neurons. *Neuropsychopharmacology* **40**, 632–639 (2015).
45. Morairty, S. R. *et al.* A role for cortical nNOS/NK1 neurons in coupling homeostatic sleep drive to EEG slow wave activity. *Proc. Natl. Acad. Sci.* **110**, 20272–20277 (2013).
46. Gerashchenko, D. *et al.* Identification of a population of sleep-active cerebral cortex neurons. *Proc. Natl. Acad. Sci.* **105**, 10227–10232 (2008).
47. Fenno, L. E. *et al.* Targeting cells with single vectors using multiple-feature Boolean logic. *Nat. Methods* **11**, 763–772 (2014).
48. Paul, A. *et al.* Transcriptional Architecture of Synaptic Communication Delineates GABAergic Neuron Identity. *Cell* **171**, 522-539.e20 (2017).
49. Ben-Simon, Y. *et al.* A suite of enhancer AAVs and transgenic mouse lines for genetic access to cortical cell types. 2024.06.10.597244 Preprint at https://doi.org/10.1101/2024.06.10.597244 (2024).
50. Sulaman, B. A., Wang, S., Tyan, J. & Eban-Rothschild, A. Neuro-orchestration of sleep and wakefulness. *Nat. Neurosci.* **26**, 196–212 (2023).
51. Grosmark, A. D., Mizuseki, K., Pastalkova, E., Diba, K. & Buzsáki, G. REM sleep reorganizes hippocampal excitability. *Neuron* **75**, 1001–1007 (2012).

472 52. Watson, B. O., Levenstein, D., Greene, J. P., Gelinas, J. N. & Buzsáki, G. Network Homeostasis and
473 State Dynamics of Neocortical Sleep. *Neuron* **90**, 839–852 (2016).
474 53. Perrenoud, Q. *et al.* Characterization of Type I and Type II nNOS-Expressing Interneurons in the
475 Barrel Cortex of Mouse. *Front. Neural Circuits* **6**, 36 (2012).
476 54. Levenstein, D., Buzsáki, G. & Rinzel, J. NREM sleep in the rodent neocortex and hippocampus reflects
477 excitable dynamics. *Nat. Commun.* **10**, 2478 (2019).
478 55. Kleinlogel, S. *et al.* Ultra light-sensitive and fast neuronal activation with the Ca^2+-permeable
479 channelrhodopsin CatCh. *Nat. Neurosci.* **14**, 513–518 (2011).
480 56. Mathis, A. *et al.* DeepLabCut: markerless pose estimation of user-defined body parts with deep
481 learning. *Nat. Neurosci.* **21**, 1281–1289 (2018).
482 57. Vyazovskiy, V. V. *et al.* Local sleep in awake rats. *Nature* **472**, 443–447 (2011).
483 58. Volgushev, M., Chauvette, Mukovski & Timofeev, I. Precise Long-Range Synchronization of Activity
484 and Silence in Neocortical Neurons during Slow-Wave Sleep. *J. Neurosci.* **26**, 5665–5672 (2006).
485 59. Funk, C. M. *et al.* Role of somatostatin-positive cortical interneurons in the generation of sleep slow
486 waves. *J. Neurosci.* **37**, 1303–17 (2017).
487 60. Tossell, K. *et al.* Somatostatin neurons in prefrontal cortex initiate sleep-preparatory behavior and
488 sleep via the preoptic and lateral hypothalamus. *Nat. Neurosci.* **26**, 1805–1819 (2023).
489 61. Krone, L. B. *et al.* A role for the cortex in sleep–wake regulation. *Nat. Neurosci.* **24**, 1210–1215
490 (2021).
491 62. Sanchez-Vives, M. V. & McCormick, D. A. Cellular and network mechanisms of rhytmic recurrent
492 activity in neocortex. *Nat. Neurosci.* **3**, 1027–1034 (2000).
493 63. Lőrincz, M. L. *et al.* A Distinct Class of Slow (~0.2–2 Hz) Intrinsically Bursting Layer 5 Pyramidal
494 Neurons Determines UP/DOWN State Dynamics in the Neocortex. *J. Neurosci.* **35**, 5442–5458 (2015).

64. Beltramo, R. *et al.* Layer-specific excitatory circuits differentially control recurrent network dynamics in the neocortex. *Nat. Neurosci.* **16**, 227–234 (2013).

65. Chen, N., Sugihara, H. & Sur, M. An acetylcholine-activated microcircuit drives temporal dynamics of cortical activity. *Nat. Neurosci.* **18**, 892–902 (2015).

66. Veit, J., Hakim, R., Jadi, M. P., Sejnowski, T. J. & Adesnik, H. Cortical gamma band synchronization through somatostatin interneurons. *Nat. Neurosci.* **20**, 951–959 (2017).

67. Chen, G. *et al.* Distinct Inhibitory Circuits Orchestrate Cortical beta and gamma Band Oscillations. *Neuron* **96**, 1403-1418.e6 (2017).

68. Huang, P., Xiang, X., Chen, X. & Li, H. Somatostatin Neurons Govern Theta Oscillations Induced by Salient Visual Signals. *Cell Rep.* **33**, 108415 (2020).

69. Echagarruga, C. T., Gheres, K. & Drew, P. J. An oligarchy of NO-producing interneurons controls basal and evoked blood flow in the cortex. *bioRxiv* 555151 (2019) doi:10.1101/555151.

70. Zielinski, M. R., Karpova, S. A., Yang, X. & Gerashchenko, D. Substance P and the neurokinin-1 receptor regulate electroencephalogram non-rapid eye movement sleep slow-wave activity locally. *Neuroscience* **284**, 260–272 (2015).

71. Vruwink, M., Schmidt, H. H., Weinberg, R. J. & Burette, A. Substance P and nitric oxide signaling in cerebral cortex: anatomical evidence for reciprocal signaling between two classes of interneurons. *J. Comp. Neurol.* **441**, 288–301 (2001).

72. Xie, L. *et al.* Sleep Drives Metabolite Clearance from the Adult Brain. *Science* **342**, 373–377 (2013).

73. Fultz, N. E. *et al.* Coupled electrophysiological, hemodynamic, and cerebrospinal fluid oscillations in human sleep. *Science* **366**, 628–631 (2019).

74. Williams, R. H. *et al.* Cortical nNOS/NK1 Receptor Neurons are Regulated by Cholinergic Projections From the Basal Forebrain. *Cereb. Cortex* **28**, 1–21 (2017).

75. Szabo, G. G. *et al.* Ripple-selective GABAergic projection cells in the hippocampus. *Neuron* **110**, 1959-1977.e9 (2022).
76. Bocchio, M. *et al.* Sleep and serotonin modulate paracapsular nitric oxide synthase expressing neurons of the Amygdala. *eNeuro* **3**, (2016).
77. Endo, T., Yanagawa, Y. & Komatsu, Y. Substance P Activates Ca 2+ -Permeable Nonselective Cation Channels through a Phosphatidylcholine-Specific Phospholipase C Signaling Pathway in nNOS-Expressing GABAergic Neurons in Visual Cortex. *Cereb. Cortex* **26**, bhu233 (2014).
78. Goldey, G. J. *et al.* Removable cranial windows for long-term imaging in awake mice. *Nat. Protoc.* **9**, 2515–2538 (2014).
79. Osborne, J. E. & Dudman, J. T. RIVETS: A Mechanical System for In Vivo and In Vitro Electrophysiology and Imaging. *PLOS ONE* **9**, e89007 (2014).
80. Stringer, C. *et al.* Spontaneous behaviors drive multidimensional, brainwide activity. *Science* **364**, 255 (2019).
81. Varin, C., Luppi, P.-H. & Fort, P. Melanin-concentrating hormone-expressing neurons adjust slow-wave sleep dynamics to catalyze paradoxical (REM) sleep. *Sleep* **41**, zsy068 (2018).
82. Traut, J. *et al.* Effects of clozapine-N-oxide and compound 21 on sleep in laboratory mice. *eLife* **12**, e84740 (2023).
83. Yüzgeç, Ö., Prsa, M., Zimmermann, R. & Huber, D. Pupil Size Coupling to Cortical States Protects the Stability of Deep Sleep via Parasympathetic Modulation. *Curr. Biol.* **28**, 392-400.e3 (2018).
84. Pachitariu, M. *et al.* Suite2p: beyond 10,000 neurons with standard two-photon microscopy. 061507 Preprint at https://doi.org/10.1101/061507 (2017).
85. Pachitariu, M., Sridhar, S. & Stringer, C. Solving the spike sorting problem with Kilosort. 2023.01.07.523036 Preprint at https://doi.org/10.1101/2023.01.07.523036 (2023).

86. Senzai, Y., Fernandez-Ruiz, A. & Buzsáki, G. Layer-Specific Physiological Features and Interlaminar Interactions in the Primary Visual Cortex of the Mouse. *Neuron* (2019) doi:10.1016/J.NEURON.2018.12.009.

Materials and Methods

Mice

All animal handling and maintenance was performed according to the regulations of the Institutional Animal Care and Use Committee of Albert Einstein College of Medicine (Protocol # 00001393) and SRI International (Protocol 01026). $Sst^{flp\ +/+}$; $Nos1^{creER\ +/-}$ and $Sst^{flp\ +/-}$; $Nos1^{creER\ +/-}$ animals were used interchangeably in this study with no differences detected between the two groups ($Nos1^{creER}$: Jax # 014541, Sst^{flp}: Jax # 031629). $Nos1^{creER\ +/-}$ animals were crossed with $Sst^{flp\ +/+}$ animals to obtain $Sst^{flp\ +/-}$; $Nos1^{creER\ +/-}$ animals and $Sst^{flp\ +/-}$; $Nos1^{creER\ +/+}$ were crossed with $Sst^{flp\ +/+}$ animals to obtain $Sst^{flp\ +/+}$; $Nos1^{creER\ +/-}$ animals. $Sst^{flp\ +/+}$; $Nos1^{creER\ +/-}$ animals were crossed with Ai210 $^{+/+}$ animals (gift from Allen Institute) [49], to obtain animals for *in vivo* imaging experiments. $Chodl^{cre\ +/+}$ animals (gift from Allen Institute) [49] were also used for *in vivo* imaging experiments and crossed with $Sst^{flp\ +/+}$ or $Sst^{flp\ +/-}$ animals. For chronic optogenetic studies, Sst^{flp} ; $Nos1^{creER}$ mice were bred with Ai80 mice (Jax #025109) to produce Sst^{flp} ; $Nos1^{creER}$; Ai80 mice. Both adult male and female mice above P50 were used in this study. Animals were kept under a 12h light/dark cycle (lights on 7am) and were maintained under standard conditions.

Cell type classification and sequencing

Data retrieved from [49].

Surgical procedures

Mice were anesthetized with isoflurane (5% by volume for induction and between 1 and 2% for maintenance), placed on a stereotaxic frame, and kept warm with closed loop heating pad. For pain management, animals were given meloxicam at 2.5 mg/kg and local lidocaine on the scalp. After a single midline incision of the skin, we minimized brain damage by performing burr holes, keeping a thin layer of the bone intact where the glass micropipettes could penetrate. The following DV values refer to brain surface.

For morphological reconstructions, a single viral vector injection of 500 nL was performed through a burr hole drilled at AP -3.3, ML ±2.7 to target primary visual cortex (V1) or at AP -1, ML ±3 to target primary somatosensory cortex (S1).

For optogenetic related surgery, 4 burr holes were drilled centered over V1 (AP -3.3, ML ±2.7) spaced ~1mm apart, and positioned to avoid blood vessels visible through the skull. 500nL of virus was injected into each burr hole split across two levels (DV -0.25 and DV -0.55) for a total of 2µL of virus.

For calcium imaging related surgery, animals were also administered with dexamethasone at 4mg/kg 1h prior craniotomy. A 3mm craniotomy was made over V1, and if applicable, virus was injected in the center of this craniotomy while the brain was kept moist with hydrated gelatin surgical foam. Then a cranial window was placed over the opening and sealed to the skull with cyanoacrylate glue. The cranial window consisted of a stack of 3 coverslips: two 3mm #1 glass coverslip (Warner Instruments) attached with Norland Optical Adhesive #71 to a 5mm glass coverslip allowing the 3mm glass to sit against the brain discouraging bone regrowth [78].

For whole neocortex targeting injections, 22 burr holes were split bilaterally and 400nL of viral vectors were injected at the following coordinates: AP +1,ML ±3, DV -1; AP +1, ±1.8, DV -0.4; AP -0.5, ML ±3.8, DV -1.5; AP -0.5, ML ±2.6, DV -0.4; AP -2, ML ±4, DV-1.2; AP -2, ML ±3.2, DV -

0.3; AP -2, ML ±1.2, DV -0.3; AP -3.5, ML ±3.5, DV -0.3; AP -3.5, ML ±2, DV -0.3 and 800nL of viral vectors were injected at the following coordinates: AP 2.5, ML ±1.2, DV -1; AP 0, ML ±1, DV -0.5.

Injections were performed using a Nanoject III system at a rate of 1 or 2nL/seconds through glass micropipettes that were pulled and then ground to bevel with 40µm diameter with a Naragishe diamond wheel. At minimum 2 weeks after surgery, animals were injected with a 5-day course of tamoxifen (Thermo Scientific) to allow the CreER recombination. A stock of 20mg/mL tamoxifen dissolved in corn oil was injected intraperitoneal (i.p.) at 0.1mg tamoxifen/g of mouse over the course of 5 days. Mice were left to build expression for a minimum of 4 weeks before use.

Finally, for calcium imaging and whole neocortex chemogenetics experiments, a separate burr hole was made in contralateral V1 and a made-in-house microwire array, used for measuring local field potentials (LFP), was inserted. The LFP wires consisted of 5 to 8 tungsten wires of 50µm spanning from middle layers of V1 into CA1. A tungsten ground wire attached to a gold pin was inserted into the cerebellum and a headpost was added [79]. Everything was cemented onto the skull with Optibond or Super-Bond and dental cement.

The following AAV viral vectors were used in this study between 10e12 - 10e13 vg/ml:

AAV vector	Serotype	Source
Ef1a-CreOn/FlpOn-oScarlet	8	provided by the lab of K. Deisseroth
Ef1a-CreOn/FlpOn-GCaMP6m	8	provided by the lab of K. Deisseroth
hSyn-CreOn/FlpOn-ChR2-EYFP	DJ	UNC vector core
EF1a-fDIO-mCherry	5	addgene (#114471)
nEF-CreOn/FlpOn-hM3Dq-mCherry	8	provided by the lab of K. Deisseroth

Immunohistochemistry

Animals were perfused transcardially with ice cold 4% paraformaldehyde (PFA) and brains were dissected from the animal to be placed in a 4% PFA for 1 hour at 4°C. Brains were embedded in OCT after sucrose cryoprotection then cryosectioned at 20µm and adhered to glass slides. To begin staining, slides with incubated in a 1.5% Donkey serum, 1% Triton-x-100 blocking solution for 1 hour. Primary antibodies were incubated overnight followed by washes and incubation for 1 hour in secondary antibody solutions.

Antigen target	Working concentration	Vendor	Product Number
Somatostatin (Sst)	1:250	Millipore	MAB354
Somatostatin-14 (Sst)	1:1000	Pennisula	T-4103
Neuronal nitric oxide synthase (Nos1)	1:500	Abcam	ab1376
GFP (reactive against EYFP)	1:500	Invitrogen	A-111222
RFP (reactive against mCherry)	1:250	Chromotek	5f8

Morphological reconstructions

Animals were injected with 500nL of Ef1a-CreOn/FlpOn-oScarlet and allowed to express for 1 month after tamoxifen induction. Mice cryosectioned as described above, with uniform sampling throughout the entire brain. Tissue sections were mounted with Prolong Gold with DAPI (Thermofisher) and imaged on a Zeiss Axioscan microscope.

Imaged brain sections were aligned to the Allen Common Coordinate Framework using Neuroinfo software (MBF Bioscience) using the *Brainmaker* workflow. Labelled neuronal arbor in aligned tissue was then reconstructed within single sections using Neurolucida 360 (MBF Bioscience). Density measurements for individual areas were made by calculating the total path length of reconstructed arbor within that area divided by the volume of the area (the 2D area within section multiplied by section thickness).

Tissue clearing and light sheet imaging

Animals were prepared as described above for morphological reconstruction. Animals were then transcardially perfused with ice cold 1xPBS followed by 4% PFA. Brains were then dissected and post fixed in 4% PFA at 4°C for 24hr. Brains were processed with SHIELD reagents (Life Canvas) before beginning active tissue clearing using the SmartBatch+ system (Life Canvas) using manufacturer protocols. Tissue was RI matched using EasyIndex (Life Canvas) and imaged on SmartSPIM light sheet microscope (Life Canvas) with a 3.9x magnification objective (NA: 0.2, Thorlabs manufactured modified by Life Canvas). Data aligned to the Allen CCF using NeuroInfo (MBF Biosciences).

Slice electrophysiology and optogenetically evoked inhibitory postsynaptic currents (oIPSCs)

Acute coronal slices of the visual cortex were prepared from adult $Sst^{flp\ +/+}$; $Nos1^{creER\ +/-}$ mice of either sex injected with AAV CreOn/FlpOn-ChR2-EYFP. Mice were anesthetized with isoflurane and intracardially perfused with ice cold cutting solution containing (in mM) 90 sucrose, 60 NaCl, 5 $MgCl_2$, 2.75 KCl, 1.25 NaH_2PO_4, 1.1 $CaCl_2$, 9 Glucose, 26.5 $NaHCO_3$, 3 Na-pyruvate, 1 Na-ascorbate, equilibrated with 95% O_2 and 5% CO_2 (osmolality adjusted to ~300 mOsm/kg). The brain was rapidly dissected and cut into 250 µm thick coronal slices in the same solution on a vibratome (VT1200S, Leica). Slices were then transferred to 34°C warm artificial cerebrospinal fluid (ACSF) containing (in mM) 120 NaCl, 25 $NaHCO_3$, 1.25 NaH_2PO_4, 3 KCl, 1.2 $MgCl_2$, 1.2 $CaCl_2$, and 11 glucose, 3 Na-pyruvate, 1 Na-ascorbate equilibrated with O_2 and 5% CO_2 and incubated for 20 min. Slices were then kept at room temperature until recording for up to 6 hours.

Putative postsynaptic neurons were recorded across all cortical layers at ~32 °C with an internal solution containing 15 CsCl, 120 CsGluconate, 8 NaCl, 10 HEPES, 2 MgATP, 0.3 NaGTP, 0.2 EGTA, and 2 mg/ml biocytin for post hoc anatomical analysis (pH adjusted to 7.2 with CsOH, osmolality adjusted to 290 mOsm/kg), the reversal potential for chloride was ~ -44 mV and GABAergic currents were recorded at +40 mV holding potential. Visually guided whole-cell recordings were obtained with patch pipettes of ~3 MΩ resistance pulled from borosilicate capillary glass (BF150-86-10, Sutter Instrument, Novato, CA). Electrophysiology data was acquired using a Sutter dPatch amplifier (Sutter Instruments), digitized at 10 kHz and filtered at 5 kHz. oIPSCs were evoked with 0.5 msec long whole-field blue light pulses (CoolLED) and a frequency of 0.2 Hz. To isolate inhibitory currents in voltage-clamp the following receptor antagonists were added to the bath solution (in µM): 2 R-CPP, 5 NBQX, 1.5 CGP to block NMDA, AMPA and GABAB receptors. To confirm GABAergic identity oIPSCs were blocked with 50 µM

SR95531 in some experiments. To confirm oIPSCs are monosynaptic, 0.5 µM TTX and 100 µM 4AP were included in the bath solution in a subset of experiments. All drugs were purchased from Abcam (Cambridge, MA) and Tocris (Bristol, UK). After recording, the patch pipette was withdrawn slowly to allow resealing of the membrane and slices fixed in 4% PFA overnight. Biocytin was labeled with streptavidin-Alexa 647 according to standard protocols. Confocal z-stacks of streptavidin-labelled neurons and fluorescently labeled Sst-ChodI fibers were taken on a Zeiss LSM 880 microscope at 1-2 µm increments. Z-stacks were processed in ImageJ and their position in the cortex recorded.

Habituation and head restraint

Animals were briefly habituated to handling for several days prior to surgery. Animals were allowed to recover for 2 days before continuing habituation to handling. After a minimum of a week post implantation, animals were gradually exposed to the head fixation apparatus (https://doi.org/10.25378/janelia.24691311) that consists of a low-friction rodent-driven belt treadmill. Headfixation times were gradually increased over the course of 2 weeks until animals were comfortable with multi-hour headfixation sessions.

To promote sleep while headfixed, we allowed the animal multiple habituation sessions on the recording rig before data collection. We ensured that the treadmill was oriented horizontally without slope with appropriately adjusted distance between the head fixation level and treadmill, that the set up was thoroughly cleaned to minimize odors from other animals, and provided a radiant heat lamp.

Videography

Video of mice was acquired at 30Hz using Blackfly machine vision ethernet enabled cameras (FLIR) equipped with a Basler lens (model c125-1620-5m) for headfixed experiments and with a Computar lens (TG4Z2813FCS-IR 0.33-Inch) for freely moving experiments. Rigs were illuminated with infrared LED arrays similar to methods described previously [80]. The camera was configured to send TTL pulses to synchronize videography with other data streams.

In vivo 2 photon calcium imaging

GCaMP was expressed using either an AAV-CreOn/FlpOn-GCaMP6m viral vector or via transgene using the Ai210 mouse line (a Cre and Flp dependent GCaMP7f). No substantial differences were noted between the two groups. Animals were imaged on a custom Bergamo 2 photon microscope coupled to a Ti:Sapphire laser (Mira 700, Coherent). Emitted light was collected though a 10x 0.5 NA long working distance objective (TL10X-2P, ThorLabs). Images were typically acquired at 1.4 frames/second with a resolution of 512x512 pixels with ThorImage software (ThorLabs). Data streams were synchronized using TTL pulses collected on an RHD USB Interface Board (Intan Technologies) at 20kHz. Prior to imaging, novel objects were placed in the animal's home cage, 1 per hour for 4 hours, to promote exploration and later facilitate sleep during imaging.

Acute in vivo electrophysiology and optogenetics

Animals were injected with AAV CreOn/FlpOn-ChR2-EYFP and implanted with headposts as described above. After expression, tamoxifen induction, and treadmill habituation, the animal was

administered with dexamethasone at 4mg/kg 1h prior craniotomy. A ~3mm craniotomy was made over the injection site (V1).

A 64 channel linear silicon probe (H3 probe, Cambridge Neurotech) physically coupled to a tapered optical fiber was slowly (1µm/sec, over ~20 minutes) inserted into V1. The craniotomy was kept moisturized during the recording by places a small volume of silicon oil on the surface of the brain. State measurements were made as described below. Between recording days, the craniotomy was protected with Kwik-cast silicon elastomer (World Precision Instruments). Mice were recorded once per day for 3-4 days.

Recordings were split into blocks of ~30 minutes of spontaneous periods (without stimulation) and ~30 minute periods of stimulation. Several different types of stimulation were used including sinusoids (1Hz, 4Hz, 10Hz, 40Hz), flat pulses, and white noise, all lasting 30 seconds followed by 30 seconds of inter trial interval (ITI). Blue light was provided by a fiber coupled LED (MF470F4, Thorlabs). Signals to control LED light intensity were generated using custom written MATLAB software and delivered to NI-Daq card (NI-PCIe-6323) to be output to the LED control box (LEDD1B, Thorlabs). No light artifacts are detected in our recordings.

Data was acquired using an Intan RHD2000 interface board at 20kHz.

Chronic optogenetics

We instrumented 3 Sst^{flp} ; $Nos1^{creER}$; Ai80 mice for EEG/EMG recordings with nuchal EMG leads and occito-parietal EEG leads and implanted 5 blue LEDs (470 nm, 3 mm diam; #RL3-B4830, Super Bright LEDs Inc., St Louis, MO) onto the skull (2 frontal, 2 parieto-lateral and one medial location) of each mouse after thinning the bone under each LED with a 4mm drill bit. The EEG/EMG leads as well as the power cables for the LEDs were connected to a 6-channel commutator (Pinnacle Technology, Inc). LED stimulation (17-25 mW/LED) occurred using a custom battery-operated, low pass (t = 0.2 msec) power supply controlled via a solid state relay (#DC60MP, Opto 22, Temecula, CA) by TTL pulses generated by a TDT System 3 also used for data acquisition (Tucker Davis Technologies, Alachua, FL). The stimulation protocol delivered 1sec pulses every other sec (0.5 Hz stimulation) for 1 h during the inactive phase and recording of EEG/EMG activity started 1h before stimulation and continued for 1h after stimulation. 3 mice were treated with TMX (300 mg/Kg, orally) 8 weeks prior to the experiments.

Freely moving behavioral assay

Animals were injected with AAV nEF-CreOn/FlpOn-hM3Dq-mCherry or control EF1a-fDIO-mCherry and implanted with LFP wires as described above. The experiment was performed during the light phase of the day and all animals were single housed post-surgery. Mice were allowed to habituate to wired tethering to a 16-channel digital headstage with accelerometer (Intan Technologies) and connected to a motorized commutator (Doric Lenses or Neurotek). To minimize stress and noise distraction, animals were kept in their home cage, inside an acoustic foam box for 2 hours per day for 3 to 5 days. Mice were also habituated to receiving systemic saline injections at the beginning of the session for at least 2 days before monitoring their behavioral state (“TEST”). A single time of the day was used for each individual (ZT 3, ZT 5 or ZT 7) and maintained across the entire experiment (habituation and TEST). No differences in sleep behavior were detected between the time of the day used and between animals.

Following habituation, animals received i.p. injection of either Vehicle (saline) or Clozapine N-oxide (CNO, Hello Bio) at 0.5mg/kg, a dose shown not to impact sleep of control animals lacking DREADD [81,82] and confirmed in our control experiment (Supp. Fig. 9g, Supp. Fig. 10b). The initial choice of treatment was counterbalanced between animals and the other treatment was administered the following day. Therefore, each session was paired with the opposite treatment for analysis (Vehicle *vs* CNO or CNO *vs* Vehicle, Supp. Fig. 9a). Each animal performed 2 or 4 paired sessions allowing us to obtain in total 28 sessions for each treatment from 8 mice.

LFP data was acquired at 1250kHz using an Intan RHD2000 interface board.

Behavioral state scoring

Behavioral state was divided based on a combination of the state measurements obtained. First, to score sleep states we utilized previously published and validated methods in the buzcode toolbox from the Buzsaki lab [51,52]. In brief, this method provides automatic state scoring dividing slow wave sleep (SWS) from wake using the slope of the power spectrum (large slope occurs during high delta periods of sleep), rapid eye movement (REM) is identified by periods of high theta with low electromyogram (EMG). The automatic scoring is then visualized and manually refined by experts.

In headfixed recordings, the remaining periods of wakefulness are then divided into periods of movement and quiet wake. To divide these states, we set a manual threshold on the movement of the face, extracted as facial motion energy by facemap. We noted that headfixed mice exhibited much longer periods of quiet wake compared to freely moving animals and confirm, as others have shown, that headfixed mice sleep with eyes open with similar LFP properties as when animals are freely moving (high delta during SWS, high theta during REM) [83].

Data analysis

Data were analyzed using open-source software packages and custom written MATLAB and python code.

Ex vivo patch-clamp

Electrophysiology data were analyzed using SutterPatch (written in IgorPro, Wavemetrics). oIPSCs were aligned to the light stimulus and 50-60 traces were averaged to calculate oIPSC amplitude and latency. Amplitude was measured as the positive maximum peak of the baselined oIPSC, and latency was calculated as time between the light stimulus and the 2x SD threshold crossing of the oIPSC from baseline.

Extraction of calcium activity

Acquired images were processed using Suite2p [84] to extract ROIs and fluorescence traces. DeltaF/F0 values were calculated by normalizing to a moving 10th percentile in 10 min windows as the baseline (F0).

Arousal score

Arousal score (Fig. 2b) was calculated using the *pca* function in Matlab. It corresponds to the time varying score for the first principal component of the measured state metrics. Principal component loadings calculated for each individual recording to provide robustness against measurement error for any singular state metric.

Classification of low arousal vs high arousal correlated cells

Cell types were determined in SST^{flp} ; Nos1^{creER} animals based on the correlation of deltaF/F traces with state metrics. K-means clustering (n=2) was performed on these correlation coefficients. Separately, we calculated the correlation coefficient of the deltaF/F signal with the arousal score. Cells with negative correlation coefficients (low arousal correlated) overlapped completely with the k-means low arousal cluster.

Division of high vs low Sst-Chodl cell activity epochs

DeltaF/F traces were averaged within recording and then z-scored. High activity epochs were defined as periods where activity was above 2 standard deviations from the mean and low activity was defined as 0.5 standard deviations below the mean.

Single Units and LFP extraction

Single units were isolated using Kilosort2 [85]. Figures contain data from both wide spiking and narrow spiking units as no differences were found between these groups. LFP signals were collected from the microwire array or from silicon probes by downsampling raw data to 1250 Hz. EMG signals were obtained with subsequent filter-Hilbert transform (>200 Hz band pass).

Calculation of power spectra

Power spectra were calculated using a wavelet-based spectrogram method using Morlet wavelets with a width of 5 cycles. These wavelets were generated for 100 log-spaced frequencies from 1Hz to 128Hz.

Determination of cortical depth

As shown previously, high frequency power (>500 Hz) peaks in mid layer 5 [86]. We interpolated between this layer 5 channel and the first channel outside of the brain (1.3 mm probe inserted 1.2 mm into the brain) assuming this distance, without the mechanical deformation of the brain cause by insertion of the probe, to be 700μm. With these interpolated pseudo-depths, we then defined layers borders at 100, 300, 450, 650, and 900μm.

Spiking synchrony

The cross correlation was calculated for each unit pair using default parameters from CCG.m in the buzcode package. The spike times of these units were shuffled and the cross correlation was recalculated 100 times to get a chance level. The real cross correlation was then normalized by this chance level to determine spiking co-activation.

Phase locking

The Fourier spectrum of the LFP was calculated for each spike of a particular using ft_spiketriggeredspectrum from the fieldtrip toolbox. The circular mean of the phase values at each frequency was calculated as the phase locking value. Though this measure is sensitive to spike count, with higher spikes leading to higher phase locking values, we believe this is not an issue as stimulation leads to slightly lower firing rates compared to baseline.

DOWN state detection

Down states were detected using a previously published method [54]. Briefly, the method detects a confluence of a large positive deflection in the LFP, drop in gamma band power, and a sharp drop in firing rate.

Mouse tracking

Cage position and mouse nest area were manually delimited using a compilation of frames extracted every 10 min from each video. Animal position was detected from the body center of the mouse using DeepLabCut open-source system [56]. The distance moved by the mice was extracted according to the real position of the cage. The duration spent in the nest was estimated by calculating the time of the mouse present in the nest according to the total duration of the experiment (2 hours).

Allen Brain Observatory data analysis

Sst expressing cell state correlation data was retrieved using the allensdk and querying the database for all experiments performed with Sst^{cre} and Cre-dependent GCaMP mice. Pearson's correlations were calculated between activity traces and state metrics binned in 3 second windows. Data on proportions of Sst-ChodI cells with Sst population was retrieved from the dataset presented in [32] from the web-based Brain Knowledge Platform (https://knowledge.brain-map.org/data).

The following software packages were used for analyzing the data presented in this paper:

Package name	URL	Publication
allensdk	https://github.com/AllenInstitute/AllenSDK	N/A
buzcode	https://github.com/buzsakilab/buzcode	N/A
facemap	https://github.com/MouseLand/facemap	Syeda et al 2023
suite2p	https://github.com/MouseLand/suite2p	Pachitariu et al 2017
kilosort2	https://github.com/MouseLand/Kilosort	Pachitariu et al 2023
fieldtrip	https://www.fieldtriptoolbox.org/	Oostenvald et al 2011
deeplabcut	https://github.com/DeepLabCut/DeepLabCut	Mathis et al 2018
Phy2.0 beta	https://github.com/cortex-lab/phy	N/A

Statistical analysis

Matlab (MathWorks) was used for statistical analysis. No power calculations were used to pre-determine sample sizes or to evaluate normality. Sample sizes were determined based on previous literature. Comparisons were performed using two-tailed parametric t-test (*ttest*), one-way or two-way ANOVA (*anova1*), with post hoc Bonferroni corrections for multiple comparisons. Differences in proportions were assessed using Chi-square tests (*chi2cdf*). Values and statistical test used are reported in the text and data are represented as mean ± standard error mean (s.e.m.) unless reported otherwise. Significance was set with alpha = 0.05 and was represented on graphs as the following: *P < 0.05, **P < 0.01, ***P < 0.001.

Acknowledgements.

We would like to thank Eliezyer Fermino de Oliveira for help using buzcode tools, Kevin Fisher and Kostantin Dobrenis from the Einstein Neural Cell Engineering and Imaging Core for assistance with imaging and image analysis, Andrea Velez, Cecilia Cuddy, and Neel Patel for providing morphological reconstruction annotations, and Adam Kohn, Saleem Nicola, Tiago Goncalves, and Jean Hebert for helpful guidance during these studies.

This work was supported by a NARSAD Young Investigator Award, a Simons Bridge to Independence Award, a Whitehall Award, and National Institutes of Health (NIH) grants R01EY034617, R21MH133097, R01EY034310 to RBB, by NINDS F31NS120723 to JMR, by Leon Levy Scholarships in Neuroscience 2023 20203010, NARSAD Young Investigator Award 31835 and Philippe Foundation to GT, by NIH 5R01HL059658 to TSK, by NIH 1U19MH114830-01 to H.Z, and by NIH 1S10OD030508 to Kostantin Dobrenis, Einstein NCEI core.

Author contributions.

Conceptualization: JMR and RBB. In vivo imaging: JMR and GT. Morphological reconstructions: JMR, JM, BS. In vitro patch clamp: SL, SR. Headfixed optogenetics: JMR, LS. Freely moving optogenetics: JH, TK. Freely moving chemogenetics: GT, JMR. Surgery and brain processing: JMR, GT, JM, AVL. Reagents: LEF, CR, KD, TD, BT, HZ. Initial draft: JR, GT, RBB. All authors edited and approved the manuscript.

Competing interests.

The authors declare no competing interests.

Materials & Correspondence.

Correspondence and requests for materials should be addressed to Renata Batista-Brito, renata.brito@einsteinmed.edu (R.B.B).

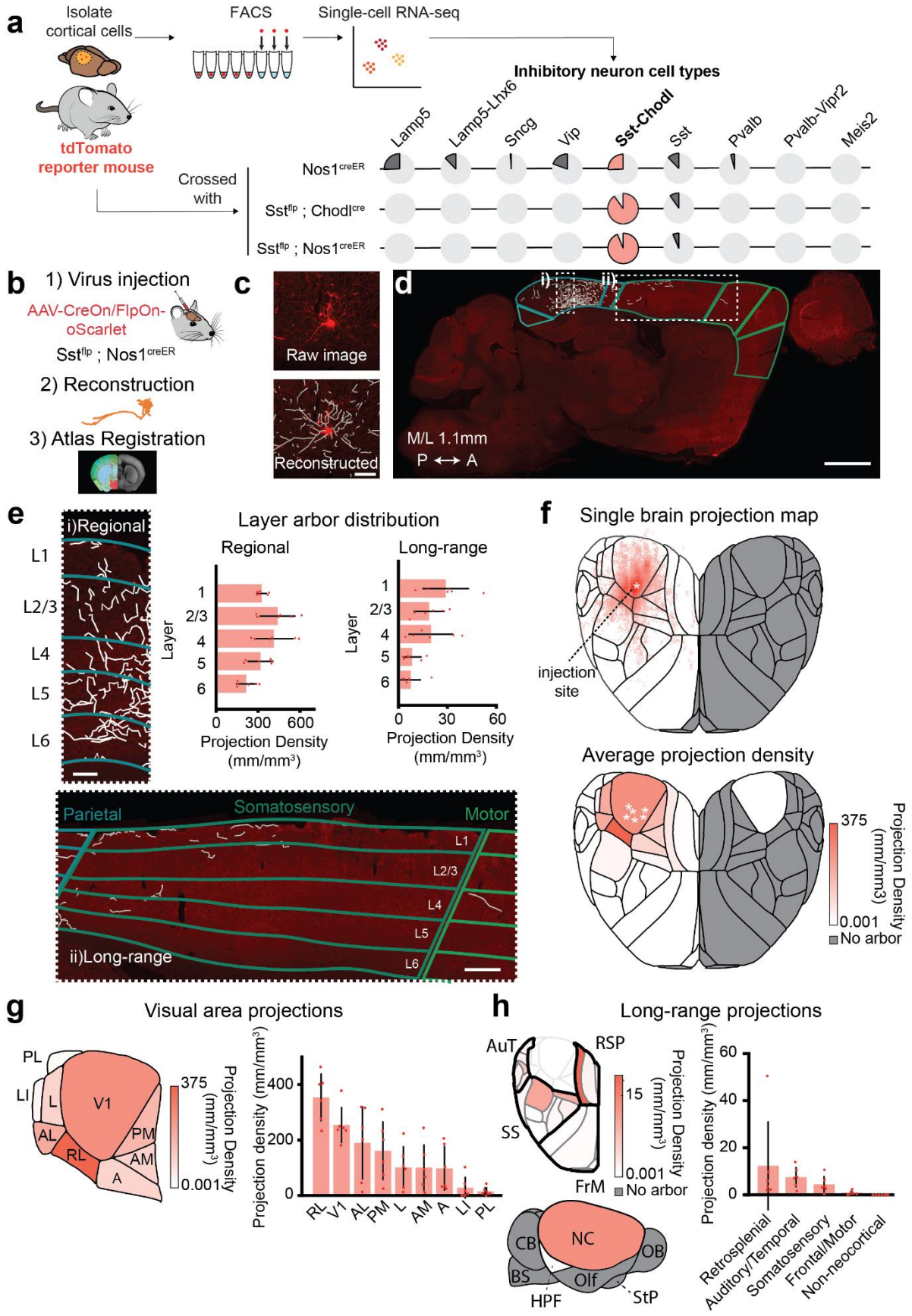

888

Figure 1 – Sst-ChodI cells from primary visual cortex have long-range projections across the neocortex. a) Experimental strategy for transcriptomic profiles and proportion of inhibitory neuron cell types labeled from single cell RNA sequencing from tdTomato reporter mice crossed with $Nos1^{CreER}$ or Sst^{flp} ; $ChodI^{cre}$ or Sst^{flp} ; $Nos1^{creER}$ mouse lines. Data from (Ben-Simon et al 2024). b) Experimental summary of an AAV-CreOn/FlpOn-oScarlet fluorophore injection into the visual cortex of Sst^{flp} ; $Nos1^{CreER}$ mice, arbor reconstruction, and atlas mapping. c) Example image of Sst-ChodI arbor with and without reconstruction (scale: 100µm). d) Thin section showing projections locally around injection site and long-range projections to frontal regions (scale: 1mm). e) Insets from d) showing (i) regional and (ii) long-range projections. Bar graphs provide quantifications of regional and interareal arbor density (scale: 100 and 200µm, respectively). f) Top: projection map from an example brain. Bottom: mean projection density across brain with inferred injection sites labelled (*). g) Schematic of visual areas showing quantification of projection density across subregions. h) Quantification of long-range projections outside of visual areas and neocortex. RL = rostrolateral visual area, V1 = primary visual area, AL = anterolateral visual area, PM = posteromedial visual area, L = lateral visual area, AM = anteromedial visual area, A = anterior area, LI = laterointermediate area, PL = posterolateral visual area, AuT = auditory/temporal cortex, RSP = retrosplenial cortex, SS = somatosensory, FrM = frontomotor cortex, CB = cerebellum, NC = Neocortex, OB = olfactory bulbs, BS = brainstem, HPF = hippocampal formation, Olf = olfactory areas, StP = Striatum/Pallidum. N = 6 mice. Data are means, bars indicate s.e.m.

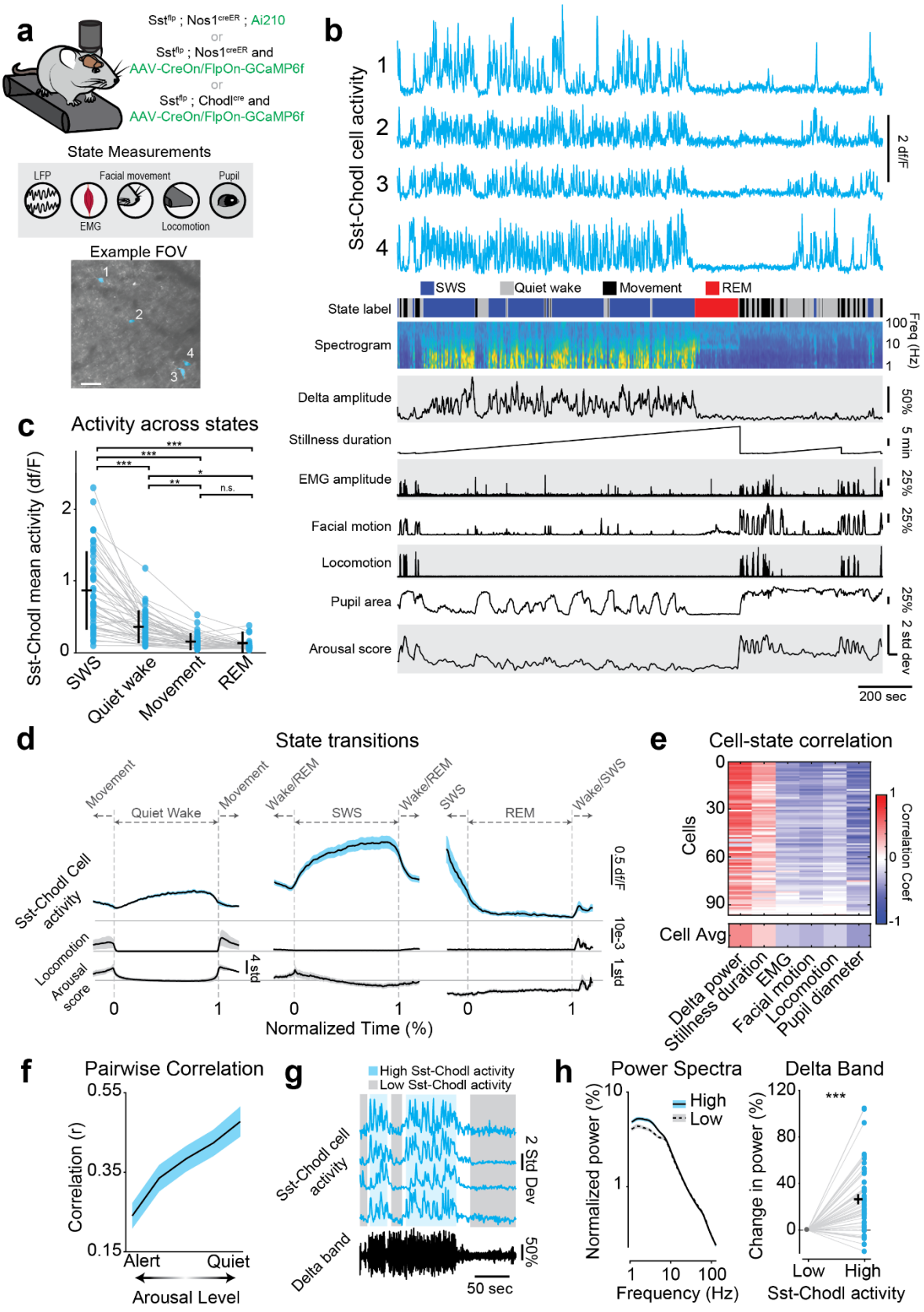

908

Figure 2 – Imaging of Sst-ChodI cells shows high activity during sleep and quiet wake. a) Schematic of GCaMP expression strategy, simultaneous imaging and state monitoring, and an example imaging field of view (FOV) with 4 Sst-ChodI cells (ROIs in blue; scale: 100 μm). b) Example data of 4 Sst-ChodI cells from a), sleep/wake states, and behavioral and physiological measures that are summarized as an arousal score. c) Mean activity of recorded cells across states. d) Mean Sst-ChodI cell activity, locomotion, and arousal level (note multiple scales) around state transitions. e) Correlation between cell activity and state measurements (i.e., delta power, pupil, etc). f) Mean pairwise correlation between cells based on arousal level. g) Example recordings during periods of high and low Sst-ChodI cell activity. h) Left: power spectra during periods of high and low Sst-ChodI cell activity. Right: quantification of delta band power change between these periods. (ANOVA $p < 0.001$, post-hoc multiple comparisons: SWS-QW $p < 0.001$, SWS-Move $p < 0.001$, SWS-REM $p < 0.001$, QW-Move $p = 0.001$, QW-REM $p = 0.010$, Move-Rem $p = 0.990$). N = 15 animals (11 Sst^{flp} ; $Nos1^{creER}$ mice and 4 Sst^{flp} ; $ChodI^{cre}$ mice), n = 97 cells (76 from $Nos1^{creER}$ cross, 21 from $ChodI^{cre}$ cross, 68 recorded across sleep and wake) and 42 pairs. ***: $p < 0.001$, **: $p < 0.01$, *: $p < 0.05$. Data are means; shading and bars indicate s.e.m.

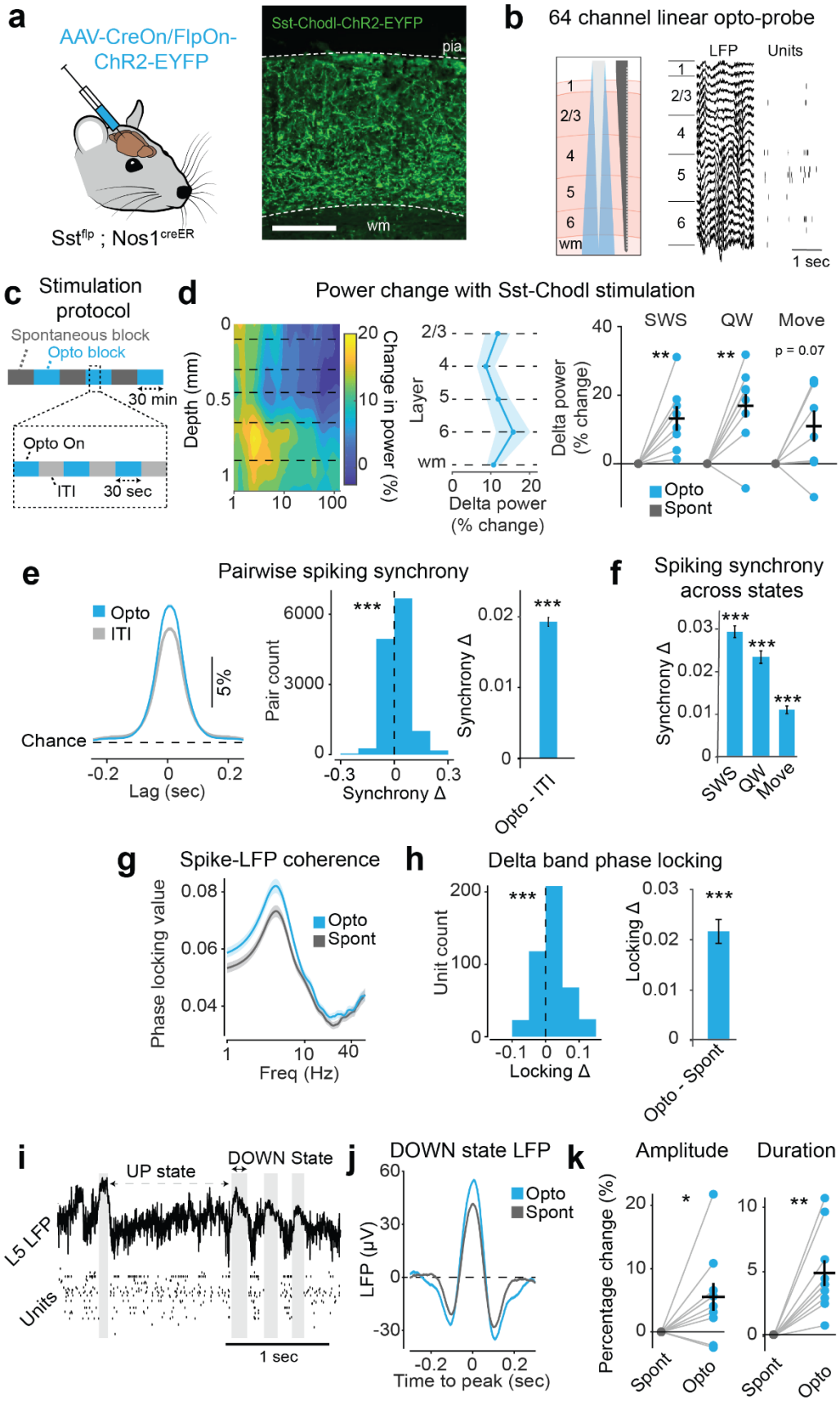

924

Figure 3 – Optogenetic activation of Sst-ChodI cells induces local network synchronization. a) Left: schematic of CreOn/FlpOn-ChR2-EYFP injections. Right: example ChR2 expression patterns (scale: 200µm). b) Schematic of linear silicon probe attached to a tapered optical fiber with example LFPs and units shown in their respective layer locations. c) Stimulation protocol schematic showing spontaneous and optogenetic stimulation (opto) blocks. Opto blocks include periods of stimulation and intertrial-intervals (ITIs). d) Left: Mean LFP power change across tissue depth. Center: change in delta power (1-4Hz) during slow wave sleep (SWS) across cortical layers. Right: delta band power change across SWS, quiet wake (QW) and movement (Move) ($p = 0.003$, 0.008, 0.069, resp., paired t-test). e) Normalized cross-correlograms (CCGs) between stimulated periods and ITIs. Left: mean CCG. Center: distribution of peak synchrony changes for each pair. Right: mean ± s.e.m. of pairwise synchrony changes ($p < 0.001$, paired t-test). f) Change in pairwise synchrony across SWS, QW, and Move ($p < 0.001$ for all, paired t-test). g) Spike-phase coherence across the LFP frequency spectrum during stimulation and spontaneous blocks. h) Distribution (left) and average (right) of unit-wise change in delta band phase locking with stimulation ($p < 0.001$, paired t-test). i) Example LFP data and single unit activity during UP and DOWN state transitions during spontaneous blocks. j) Average LFP time-locked to the peak of the DOWN state with (blue) and without (grey) optogenetic stimulation in example session. k) Change in amplitude and duration of DOWN state with optogenetic stimulation ($p = 0.021$ and $p = 0.003$, respectively, paired t-test). N = 8 sessions across 4 mice, N = 446 units and 39,804 pairs. ***: $p < 0.001$, **: $p < 0.01$, *: $p < 0.05$; ns, not significant. Data are means, shading and bars indicate s.e.m.

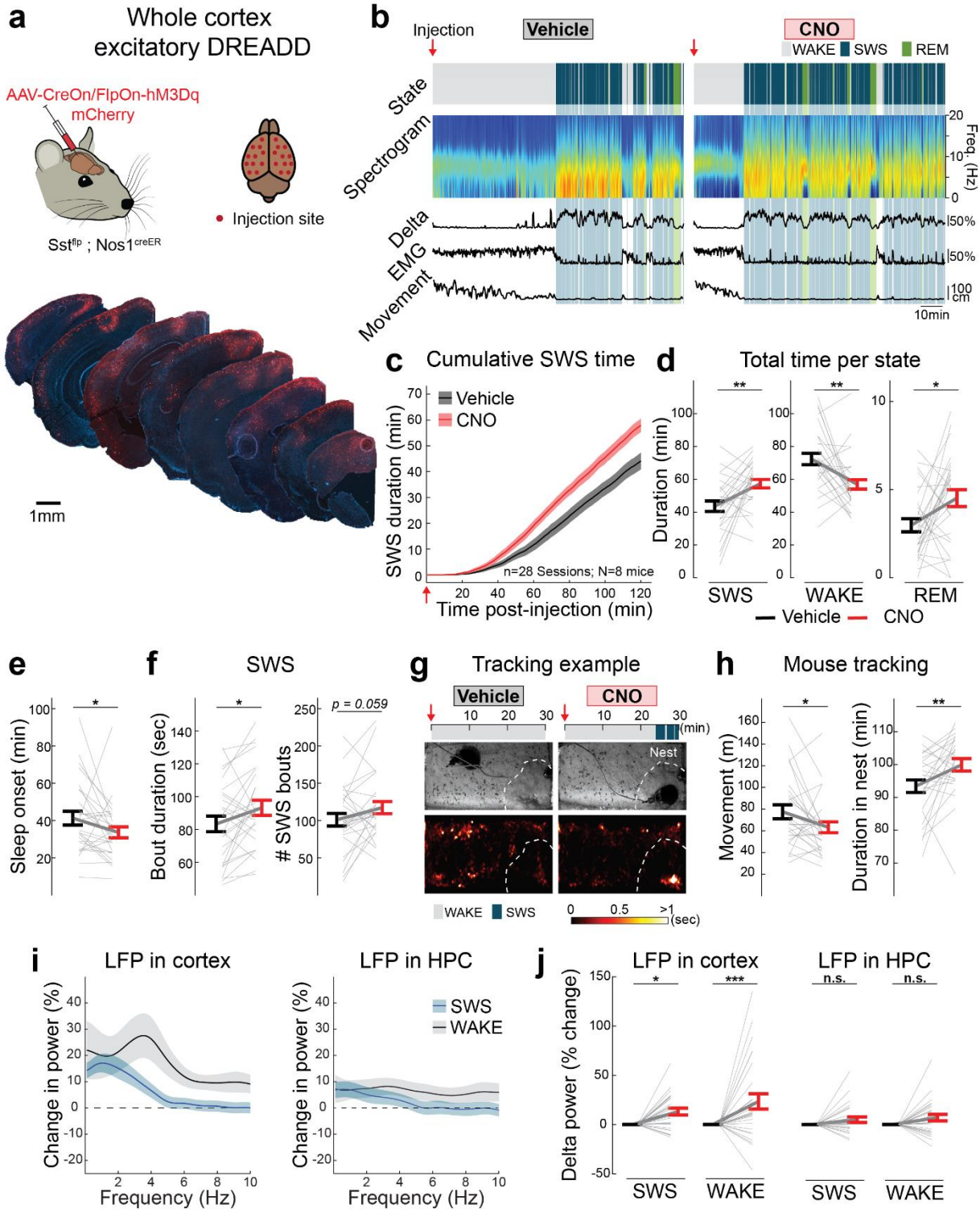

945

Figure 4 – Chemogenetic activation of neocortical Sst-Chodl neurons promotes sleep. a) Top: strategy for targeting the entire neocortex by injection of AAV-CreOn/FlpOn-hM3Dq mCherry at 22 injection sites. Bottom: example of a control brain injected with the AAV-EF1a-fDIO-mCherry vector. b) Example sessions for one mouse after systemic injection of Vehicle (left) or 0.5mg/kg CNO (right) with sleep/wake state scoring and physiological measurements. c) Cumulative SWS sleep time across sessions following Vehicle (grey) or CNO (red) injection. d) Total time spent in SWS, WAKE, and REM sleep for the 2 hours after injection (Vehicle, black; CNO, red; SWS, $p = 0.002$; WAKE, $p = 0.002$; REM $p = 0.015$, respectively). e) Latency to sleep onset ($p = 0.009$). f) SWS bout duration ($p = 0.020$) and numbers of SWS bouts ($p = 0.059$). g) Tracking example of the mouse in b) during the first 30 min following injections. Top bar: sleep/wake scoring according to the legend at the bottom of the panel. Center: images of mouse and nest (dashed white line) position in home cage. Bottom: heatmap of the animal position during the 30 min period. h) Total distance travelled ($p = 0.031$) and time in nest ($p = 0.010$) during the 2 hours post-injection. i) LFP power change from channels recorded in the neocortex (left) and in the hippocampus (HPC, right) during SWS (blue) or WAKE (grey) periods. j) Delta band (0.5-4Hz) power change during SWS sleep *vs*. wake from neocortical (SWS, $p = 0.030$; WAKE, $p < 0.001$) and hippocampal channels (SWS, $p > 0.999$; WAKE, $p = 0.585$). ***, $p < 0.001$; **, $p < 0.01$; *, $p < 0.05$; ns, not significant; paired t-test for D-F) and H) and two-way repeated ANOVA for J) with interaction $p = 0.036$; followed by Bonferroni post hoc comparisons. N = 28 sessions across 8 mice. Data are means, shading and bars indicate s.e.m.

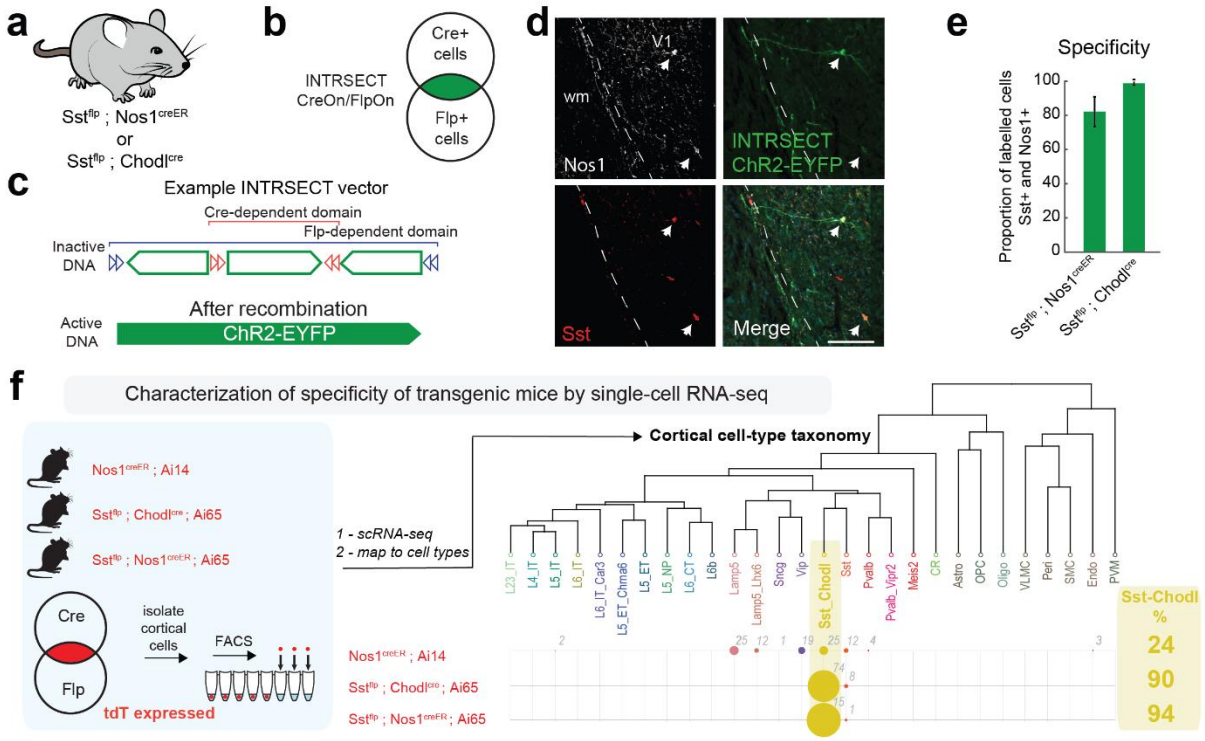

Supplemental Figure 1: Intersectional targeting of Sst-Chodl cells with high specificity. a) Mouse lines used for intersectional targeting. b) Venn diagram of cells targeted by CreOn/FlpOn vector. c) Example INTRSECT vector active only after both Cre and Flp recombination. d) Histology of ChR2-EYFP expressed in Sst-Chodl cell from the primary visual cortex (V1) with axon travelling through white matter (wm). Scale: 150µm; arrows indicate cells co-expressing Sst and Nos1. e) Proportion of cells expressing GCaMP, Sst, and Nos1 (N=62 cells from 4 Sst^{flp} ; $Nos1^{creER}$ mice and 30 cells from Sst^{flp} ; $Chodl^{cre}$ mice). f) Cortical cell-type taxonomy following single cell RNA-sequencing from three transgenic mouse lines ($Nos1^{creER}$, Sst^{flp} ; $Chodl^{cre}$ and Sst^{flp} ; $Nos1^{creER}$) crossed with tdTomato reporter lines. Numbers indicate cell count. Data from (Ben-Simon et al 2024).

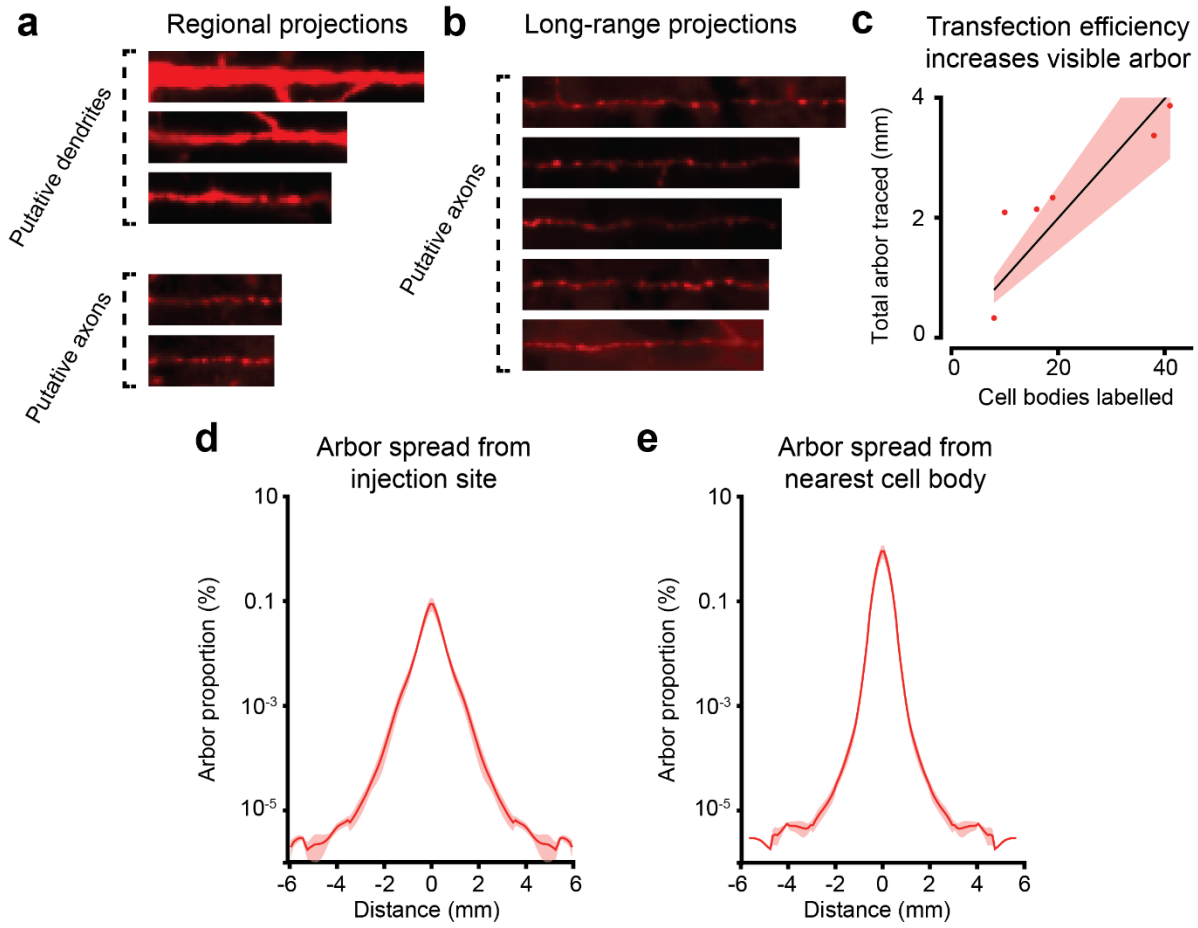

978

979 **Supplemental Figure 2: Sst-ChodI cells dendritic and axonal arbors.** a) Putative dendrites
980 and axons locally near the injection site in V1. b) Putative axons without dendrites found far from
981 injection site (outside visual areas). c) Regression line fit relating transfection strength with total
982 arbor traced. d) Arbor spread from inferred injection site travelling multiple millimeters. e) Arbor
983 spread from nearest cell body travelling multiple millimeters. Data are means; shading indicate
984 s.e.m.

985

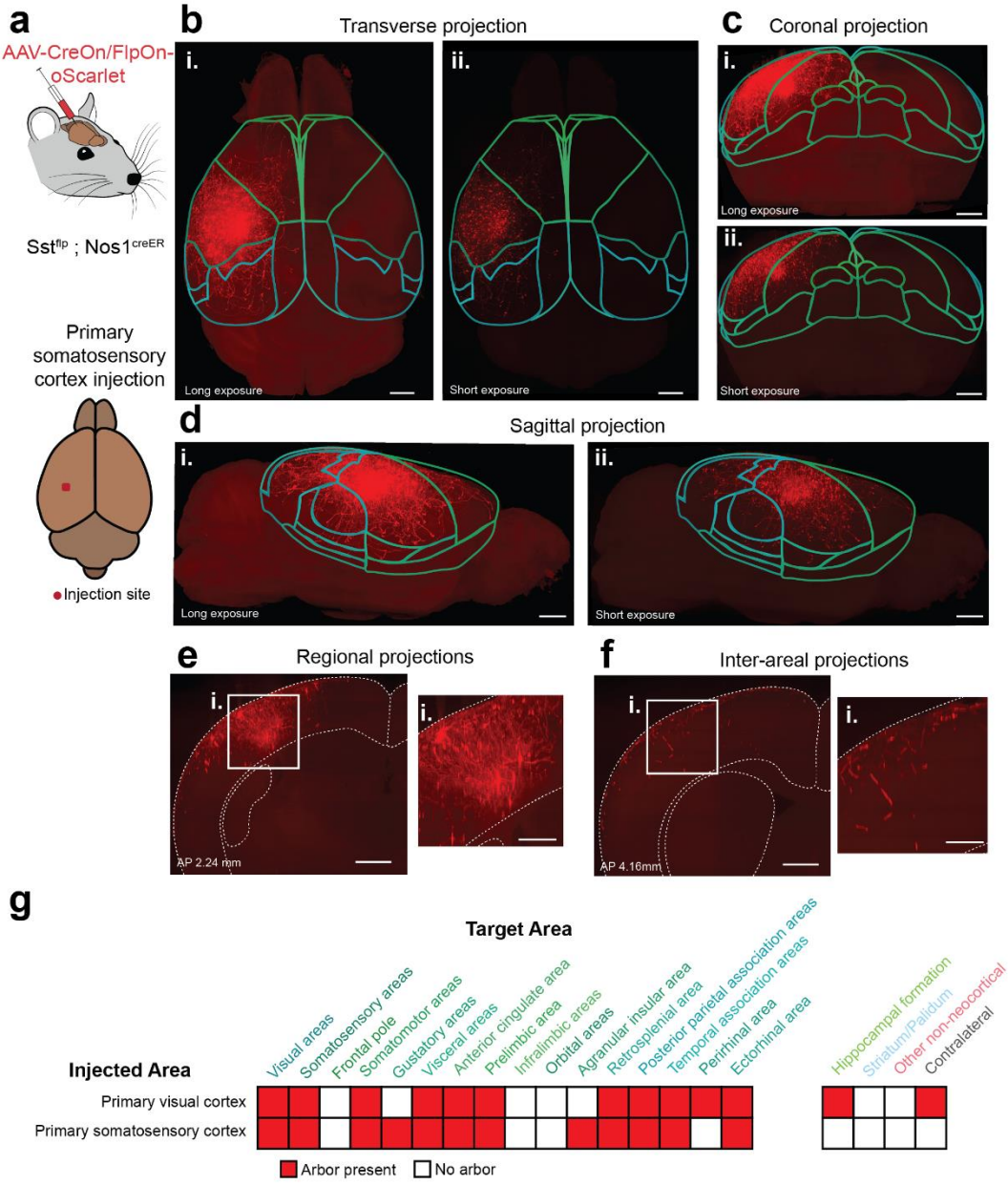

Supplemental Figure 3: Projections from Sst-ChodI cells with somata in the primary somatosensory cortex. a) Schematic of experimental design of an AAV-CreOn/FlpOn-oScarlet fluorophore injection into the primary somatosensory cortex of a Sst^{flp} ; $Nos1^{creER}$ mouse. b) Dorsal view of a cleared whole brain injected with oScarlet in the primary somatosensory cortex with (i) long or (ii) short exposure of the fluorophore. c-d) same as b) but from anterior view c) and from lateral view d). e) Coronal view around the injection site. f) Coronal view far from the injection site. Insets represent zoom in from i) noted region. g) Comparison of areas targeted by injections into the primary visual cortex *vs*. primary somatosensory cortex. a-d) scale: 1mm; e-f) scale: 0.5mm with inset scale 0.25mm.

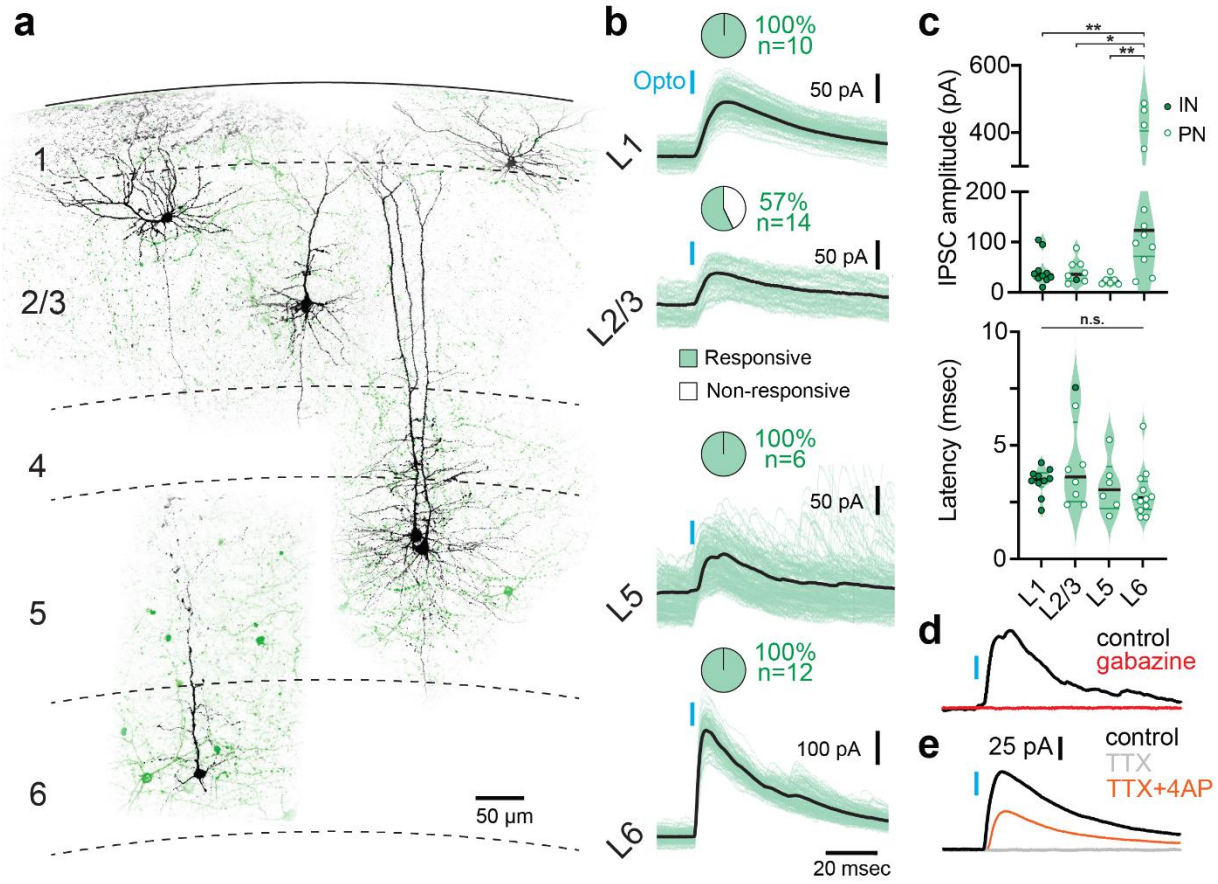

Supplemental Figure 4: Broad postsynaptic targeting of Sst-ChodI cells. a) Schematic of cortical layers 1-6 showing representative anatomical fills of postsynaptic neurons (black) with ChR2-expressing Sst-ChodI fibers superimposed (green). b) Individual oIPSCs (green) with average traces superimposed (50-60 traces, black) aligned to the light stimulus (Opto, blue). Pie charts indicate the percentage of recorded cells that responded to Sst-ChodI cell stimulation and the total number of cells recorded in each layer. c) Summary data of oIPSC amplitudes and latencies. Green circles denote putative interneurons (IN) and white circles pyramidal neurons (PN); horizontal lines denote median (black) and interquartile (green). One-way ANOVA interaction for IPSC amplitude: p = 0.001; L1 *vs* L6, p = 0.005; L2/3 *vs* L6, p = 0.013; L5 *vs* L6, p = 0.009; all other comparisons, p > 0.9; n=42 cells/N=10 animals. d) Gabazine (red, 50µM) blocks the Sst-ChodI oIPSC, indicating that it is GABAergic (same cell as L5 in b). e) Representative recording of Sst-ChodI oIPSC under control conditions (black) and in the presence of TTX (0.5 µM grey). 4AP (100 µM) recovers the oIPSC (orange), indicating it is monosynaptic. **: p < 0.01, *: p < 0.05; ns, not significant.

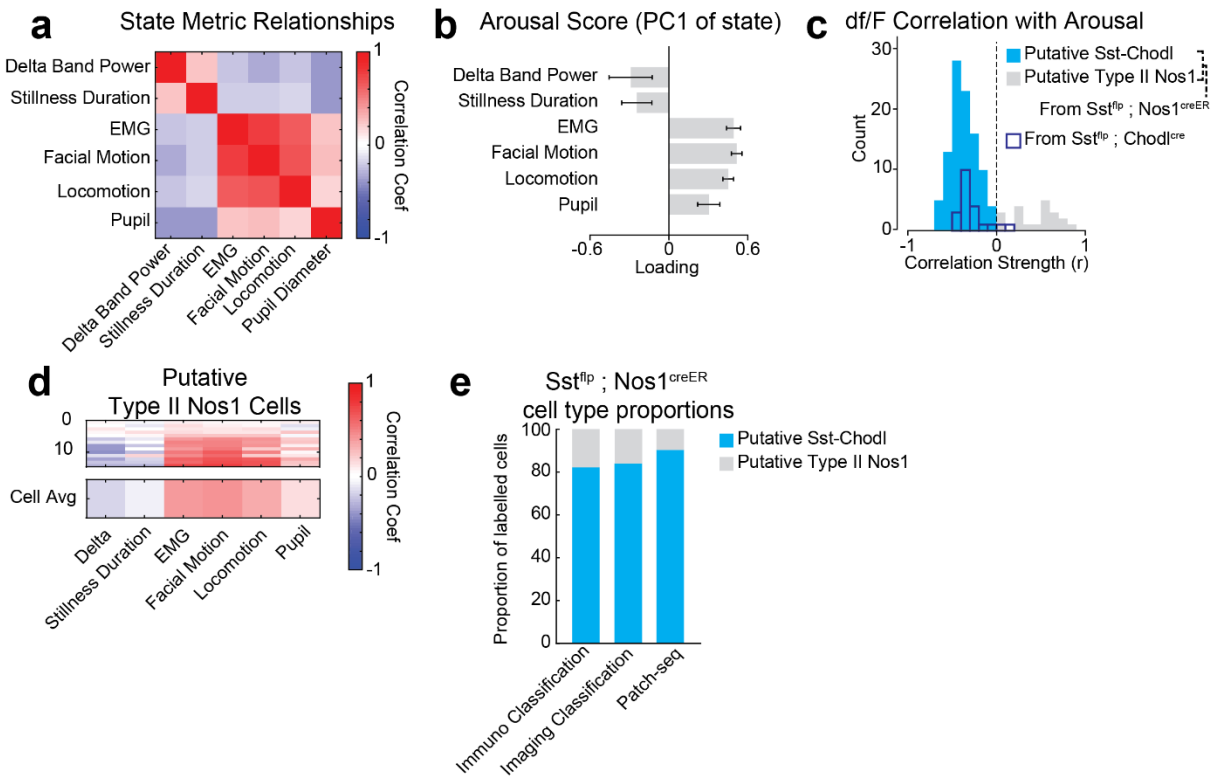

Supplemental Figure 5: Arousal score summarizing multiple measurements of state and identification of putative Type II Nos1 cells. a) Average correlation between state measurements. b) Consistent PC loadings 1 in PCA of state measurements across animals. c) Distribution of correlation coefficients between imaged cell df/F and arousal score. Cells from Sst^{flp} ; $Nos1^{creER}$ mice (full) and from Sst^{flp} ; $Chodl^{cre}$ mice (clear) are assigned by k-means clustering for each space of df/F *vs* state metric correlation. d) Correlation of putative Type II Nos1 cell activity with state metrics (N = 16 out of 111 recorded cells from 15 animals). a-d) Data related to figure 2. e) Proportion of Sst-Chodl and putative Type II Nos1 cells with identity determined by immunohistochemistry (N = 62 cells from 4 animals), imaging and activity correlation (N = 90 cells from 11 mice), and by patch-seq in Sst^{flp} ; $Nos1^{creER}$ mice crossed with Ai65 mice from Allen Brain Institute in Gouwens et al 2020 (N = 87 cells). Data are means; bars indicate s.e.m.

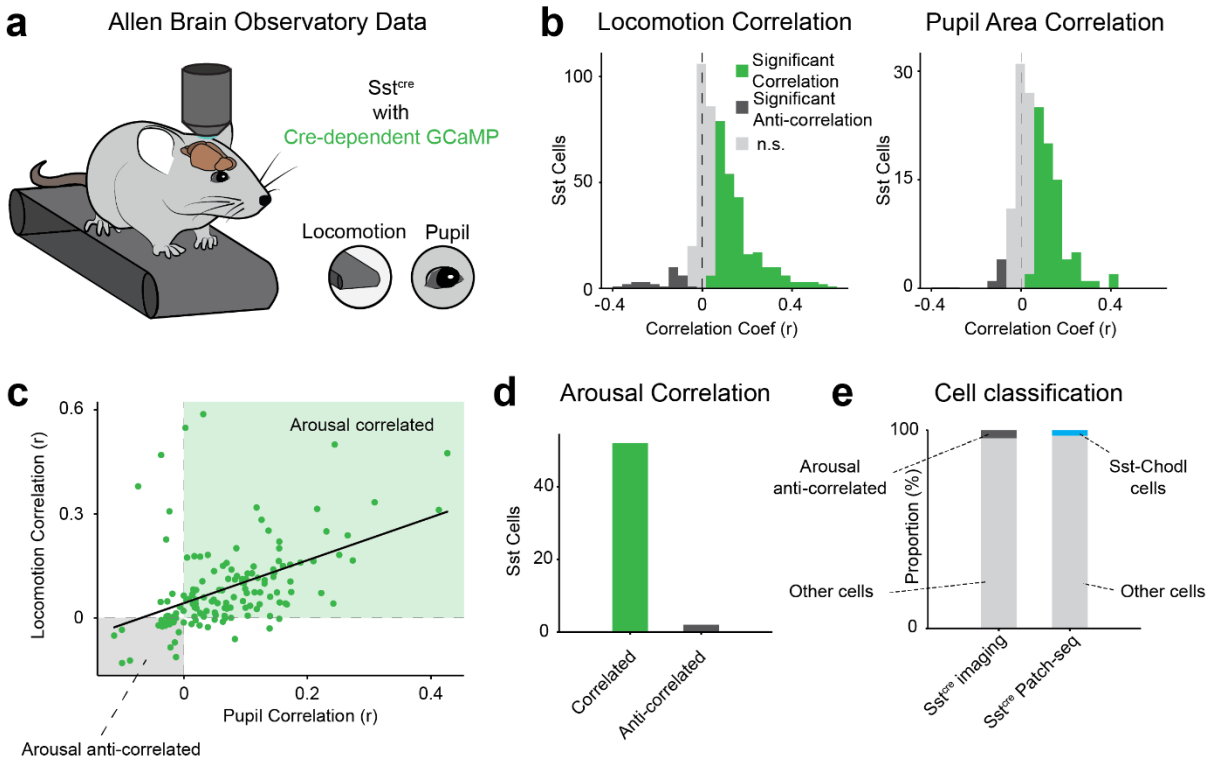

Supplemental Figure 6: Imaging of Sst cells and correlation with state metrics. a) Imaging data from Sst^{cre} mice retrieved from Allen Brain Observatory including cell activity traces, locomotion, and pupil. b) Pearson's correlation of dF/F with locomotion (right) and pupil (left), in 3 sec bins. Significant positive correlation (green), significant negative correlation (dark grey), and non-significant correlation (light grey). c) Correlation coefficient of individual cells with pupil and locomotion. Quadrant colored representing arousal correlation (positive correlation with locomotion and pupil area) and arousal anti-correlation (negative correlation with locomotion and pupil area). (Regression r = 0.46, $p < 0.001$). d) Count of significantly arousal correlated and anti-correlated Sst cells in the dataset. e) Proportion of arousal anti-correlated cells in Sst population compared to Sst-Chodl cell proportion in Allen Patch-seq data. Arousal anti-correlated cells: n=6 out of 147 Sst cells *versus* n=25 out 900 Sst cells obtained from Gouwens et al 2020 and Allen Brain Observatory respectively, Chi Square p = 0.39.

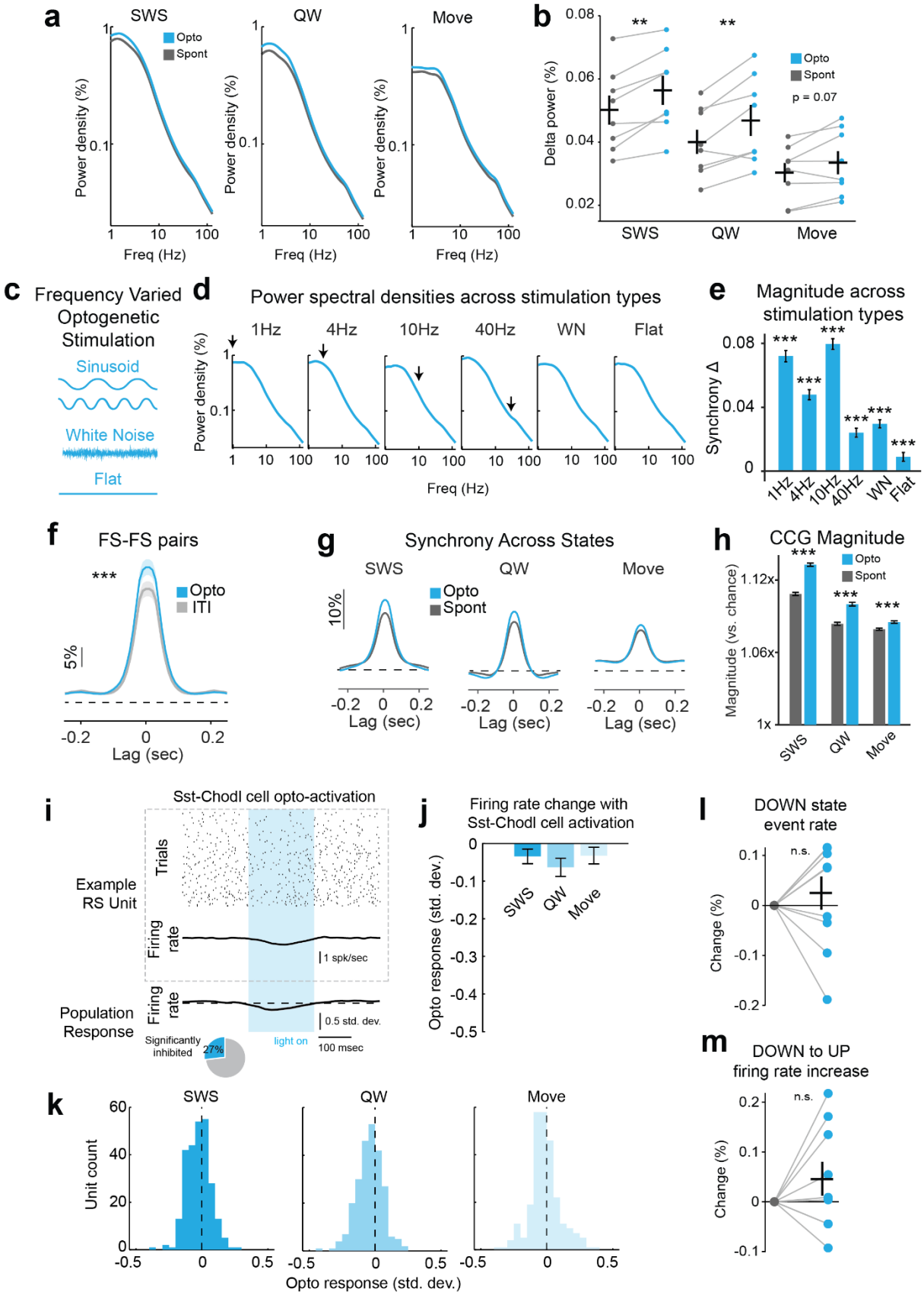

1040

Supplemental Figure 7: Stimulating Sst-ChodI cells with optogenetics increases synchrony across states and stimulation types. a) Power spectral densities during optogenetic stimulation and spontaneous periods across sleep (slow-wave sleep, SWS) and wake states (movement, Move; quiet wake, QW) with b) quantification of delta band power in the LFP ($p = 0.003$, 0.008, 0.069, respectively, paired t-test). c) Frequency-varied optogenetic stimulation schematic with sinusoidal, white noise (WN), and flat stimulation. d) Power spectral densities for all stimulation types during SWS indicating lack of non-physiological entrained oscillation at sinusoidal stimulation frequencies (arrows). e) Increase in pairwise spiking synchrony across all frequencies of stimulation tested ($p < 0.001$ for all, paired t-test). f) Fast-spiking (FS) unit pair synchrony before and during Sst-ChodI cell stimulation ($n = 476$ pairs, $p < 0.001$, paired t-test). g) Average normalized cross correlogram of spiking unit pairs during stimulation and spontaneous periods and across states with h) quantification of peak synchrony (+/- 50 msec, $p < 0.001$ for all, paired t-test). i) Example recording of the firing rate of regular spiking units (RS) during optogenetic activation of Sst-ChodI cells (blue area). 27% of all recorded neurons showed a significant decrease in firing rate. j) Change in firing rate of RS units and k) distribution of the response across sleep and wake states during optogenetic stimulation of Sst-ChodI cells. l) Change in DOWN state event rate during SWS ($p = 0.437$, paired t-test). m) Change in firing rate around DOWN to UP transition during SWS ($p = 0.201$, paired t-test). Data related to Figure 3. $N = 4$ mice. ***: $p < 0.001$, **: $p < 0.01$, *: $p < 0.05$; ns, not significant. Data are means, shading and bars indicate s.e.m.

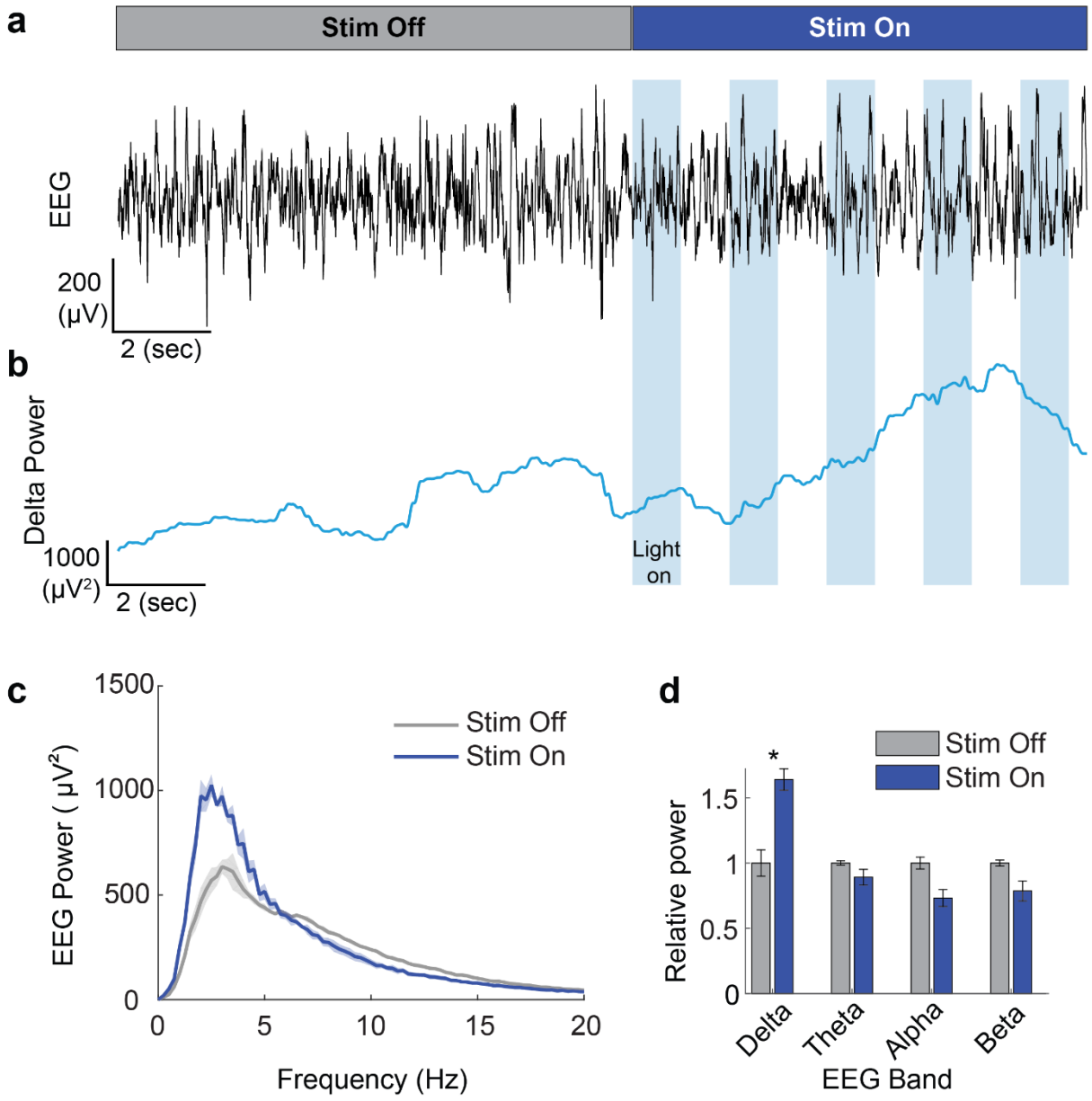

Supplemental Figure 8: Transcranial cortex-wide optogenetic stimulation of Sst-ChodI cells in freely moving animals enhances EEG delta activity during SWS. a) Example EEG trace during SWS with spontaneous (Stim off) and stimulation (Stim On) periods of a Sst^{flp} ; $Nos1^{creER}$; Ai80 mouse. Shaded blue areas indicate light on. b) Smoothed delta band power extracted from a). c) Average SWS power spectra. d) Power of the different EEG bands during SWS, normalized to the mean power without stimulation. Asterisks denote significant difference ($p = 0.032$, corrected multiple comparisons with Bonferroni t-test, N=3 animals). EEG spectrum is divided into Delta (1-4 Hz), Theta (5-10 Hz), Alpha (10-13 Hz) and Beta (13-30 Hz) bandwidths. Data are means, shading and bars indicate s.e.m.

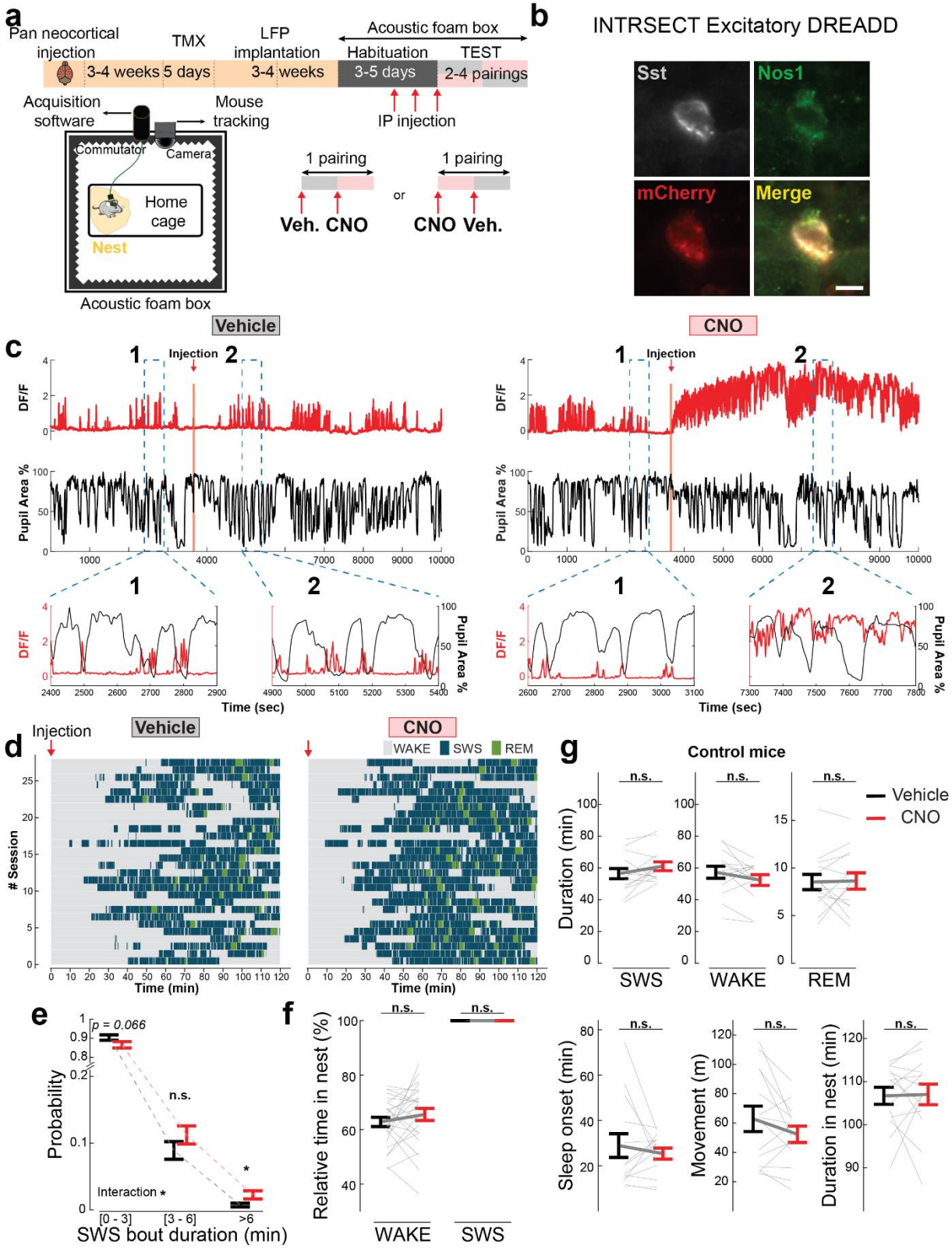

1073

Supplemental figure 9: Chemogenetic activation of neocortical Sst-ChodI cells promotes sleep. a) Experimental protocol for pan neocortical activation of Sst-ChodI activity, injection and sleep monitoring. b) Histology of an Sst-ChodI cell expressing CreOn/FlpOn excitatory DREADD tagged with mCherry. c) Example recording of the calcium activity (red) from an Sst-ChodI cell expressing excitatory DREADD and pupil area measurements (black) before and after systemic injection of Vehicle or 0.5mg/kg of CNO. After CNO injection, Sst-ChodI cell activity increases independently of the animal's arousal state. d) Hypnogram for all the sessions monitored after Vehicle and CNO injection. e) Distribution of SWS bout duration after pan-neocortical activation of Sst-ChodI cells. Two-way ANOVA interaction, $p = 0.034$; [0 – 3 min], $p = 0.066$; [3 – 6 min], $p = 0.322$; [>6 min], $p = 0.045$. f) Proportion of time spent in nest during WAKE ($p = 0.206$, paired t-test) and SWS ($p = 0.594$, paired t-test). g) Total time spent in each state (SWS, WAKE, and REM sleep), sleep onset, total distance travelled and duration in nest during the 2 hours after injection of Vehicle (black) and CNO (red) in control animals that did not express DREADD. SWS, $p = 0.076$; WAKE, $p = 0.109$; REM, $p = 0.865$; Sleep onset, $p = 0.280$, Movement, $p = 0.097$; Duration in nest, $p = 0.895$; paired t-test. N = 28 sessions across 8 mice with Sst-ChodI excitatory DREADD and N = 14 sessions across 7 control mice. *: $p < 0.05$, ns: not significant. Data are means with s.e.m.

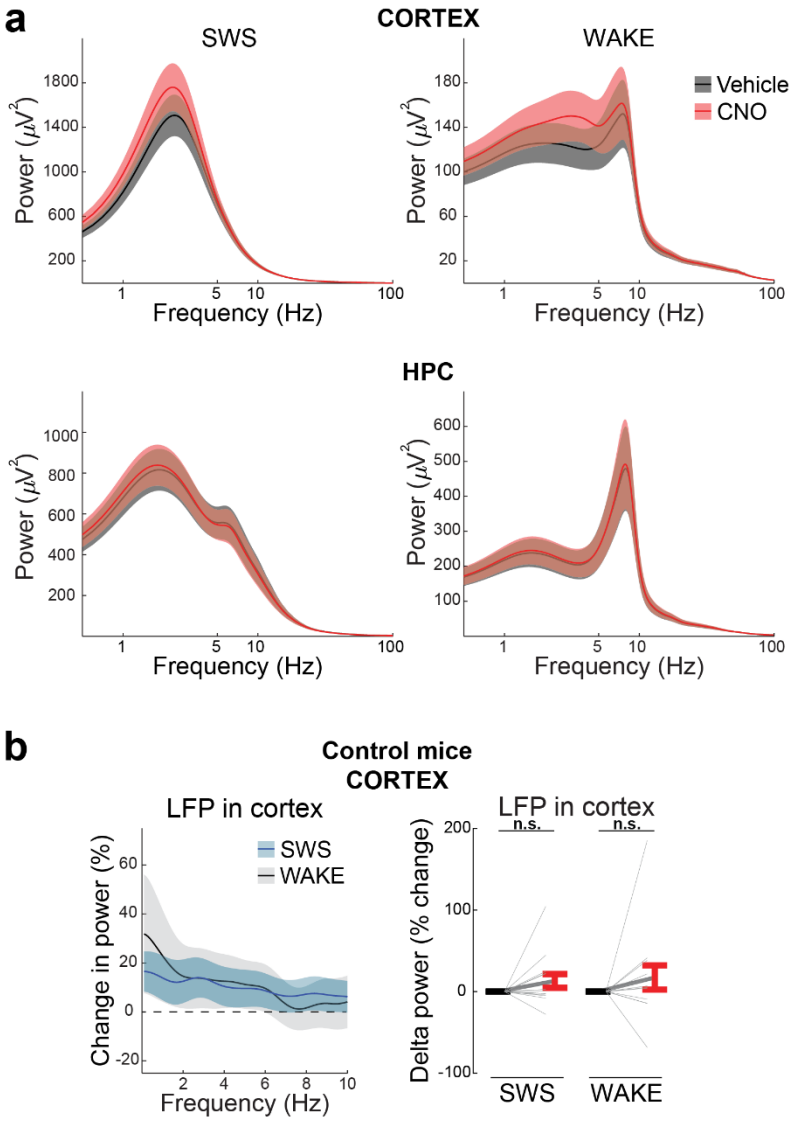

Supplemental figure 10: Pan-neocortical activation of Sst-ChodI cells increases cortical delta power.

a) Power spectral densities after Vehicle (grey) and chemogenetic stimulation (red) of neocortical Sst-ChodI cells during SWS (left) and WAKE (right) states from channels recorded in the neocortex (top) and in the hippocampus (HPC, bottom). N = 28 sessions across 8 mice. b) LFP power change and delta band (0.5-4Hz) power change during SWS and WAKE from neocortical channels recorded in control mice. ns: not significant, Two-way repeated ANOVA (interaction, p = 0.807). N = 14 sessions across 7 control mice. Data are means, shading and bars indicate s.e.m.

1104

Area Name	Mean density	Density std. dev.
rostrolateral area	353.817744	86.8542906
primary visual area	254.230876	65.5825874
anterolateral visual area	190.110085	132.862149
posteromedial visual area	161.073969	106.692083
lateral visual area	101.274409	77.2172299
anteromedial visual area	100.422502	84.620492
anterior area	97.7034925	81.273239
retrosplenial area, lateral agranular part	49.2437828	98.0013612
laterointermediate area	28.0897375	39.5950979
primary somatosensory area, barrel field	27.8738788	16.9356931
primary somatosensory area, trunk	25.4189775	24.0517205
posterior auditory area	15.8636398	14.0018957
posterolateral visual area	14.947232	15.1223005
primary somatosensory area, lower limb	5.23046765	3.22956478
primary auditory area	5.19198356	7.34538855
temporal association areas	4.7131325	3.53264572
retrosplenial area, dorsal part	4.63443433	3.403158
dorsal auditory area	4.55820316	5.11929393
retrosplenial area, ventral part	3.61808834	3.83703651
primary somatosensory area, unassigned	3.48660635	3.12185105
anterior cingulate area, dorsal part	3.39150012	4.90557255
postrhinal area	3.3136601	3.48534805
supplemental somatosensory area	2.85778752	3.15858147
primary somatosensory area, upper limb	2.8159213	2.811427
secondary motor area	1.54072935	1.4655554
primary somatosensory area, nose	1.16144038	1.72629817
primary motor area	0.99224953	0.94206136
ectorhinal area	0.70558025	1.24361704
visceral area	0.4692631	0.69785985
ventral auditory area	0.39940397	0.25300502
anterior cingulate area, ventral part	0.31308763	0.36811857
perirhinal area	0.22011255	0.53916344
primary somatosensory area, mouth	0.15346161	0.23937919
prelimbic area	0.05074395	0.12429677
agranular insular area, dorsal part	0	0
agranular insular area, posterior part	0	0

agranular insular area, ventral part	0	0
frontal pole	0	0
gustatory areas	0	0
infralimbic area	0	0
orbital area, lateral part	0	0
orbital area, medial part	0	0
orbital area, ventrolateral part	0	0

Supplemental table 1: Complete list of area projection densities. Table showing the projection density (path length/volume) of all neocortical areas from the Allen Common Coordinate framework, plus hippocampal formation areas with projections.

Supplemental video 1: Sst-Chodl cells labelled in primary somatosensory cortex. Sst-Chodl cells labelled with intersectional oScarlet AAV injected into S1 and imaged in whole mount cleared brain.

Supplemental video 2: Imaging of Sst-Chodl cell expressing excitatory DREADD prior to CNO injection. Facial videography with extracted pupil diameter visualized in yellow with simultaneous imaging of a Sst-Chodl cell (red). Blue line indicates the real time of the video. When the animal is less aroused and pupil diameter decreases, Sst-Chodl cell activity increases.

Supplemental video 3: Imaging of Sst-Chodl cell expressing excitatory DREADD after CNO injection. Facial videography with extracted pupil diameter visualized in yellow with simultaneous imaging of a Sst-Chodl cell (red). Blue line indicates the real time of the video. After CNO injection, the cell becomes highly active and the relationship between pupil diameter/arousal level and Sst-Chodl cell activity is broken.